iScience

Article

Multifunctional LA and PTMC coating for biliary stents to combat cholangiocarcinoma proliferation in obstruction

Graphical abstract

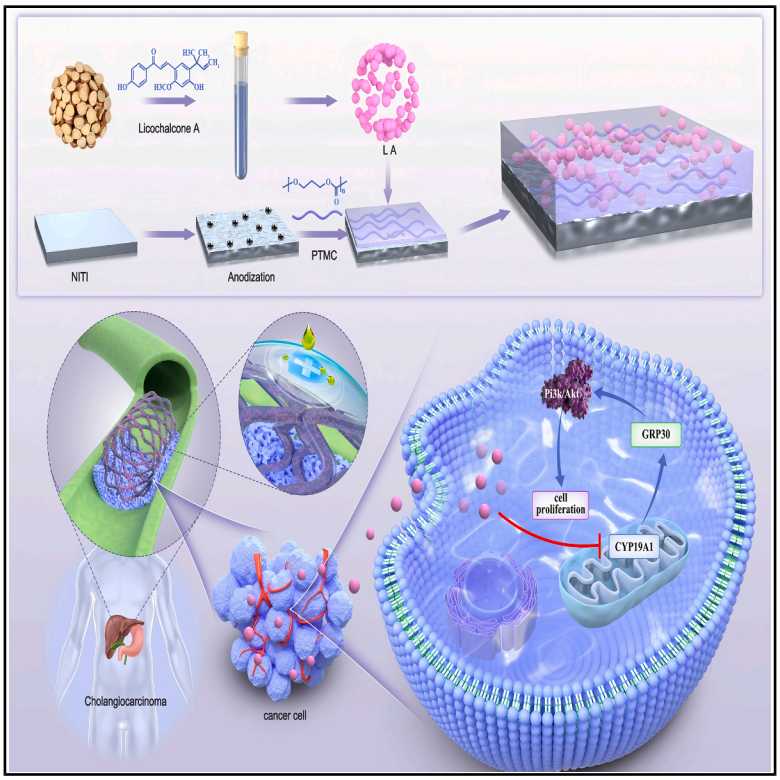

Highlights

- Novel coating integrates licochalcone A and PTMC for dual-function biliary stents
- Superior to oral delivery, achieving enhanced *in vivo* tumor suppression and bioavailability
- Targets CYP19A1 to inhibit GPR30-AKT axis, enhancing interventional therapy

Authors

Liang Jin, Yaoting Wang, Yaohui Liu, ..., Li Yu, Ling Zhang, Rui Zan

Correspondence

yuli9119@126.com (L.Y.), zhanglingwws@163.com (L.Z.), zanr@ywfudan.cn (R.Z.)

In brief

Drugs; Pharmaceutical science; Small molecule

Jin et al., 2026, iScience *29*, 116093
August 21, 2026 © 2026 The Author(s). Published by Elsevier Inc.
https://doi.org/10.1016/j.isci.2026.116093

CellPress

iScience

CellPress
OPEN ACCESS

Article

Multifunctional LA and PTMC coating for biliary stents to combat cholangiocarcinoma proliferation in obstruction

Liang Jin,[1,3,6,7] Yaoting Wang,[1,7] Yaohui Liu,[5] Qianping Mao,[1] Ben Feng,[3] Jiaxing Xin,[1] Yumei Zhang,[4] Lan Li,[1] Xiaodan Guan,[1] Xiaolong Wu,[1] Zhengtao Wang,[3] Li Yu,[1,*] Ling Zhang,[1,*] and Rui Zan[2,6,8,*]

[1]School of Medical Technology and Information Engineering & School of Life Science & School of Basic Medical Sciences, Zhejiang Chinese Medical University, Hangzhou 310053, China
[2]Yiwu Research Institute of Fudan University, Yi Wu 322099, China
[3]Shanghai Key Laboratory of Compound Chinese Medicines, Shanghai University of Traditional Chinese Medicine, Shanghai 201203, China
[4]Shanghai East Hospital Affiliated to Tongji University, Shanghai 200120, China
[5]RWTH Aachen University, 52062 Aachen, Germany
[6]School of Materials Science and Engineering, Shanghai Jiao Tong University, Shanghai 200030, China
[7]These authors contributed equally
[8]Lead contact
*Correspondence: yuli9119@126.com (L.Y.), zhanglingwws@163.com (L.Z.), zanr@ywfudan.cn (R.Z.)
https://doi.org/10.1016/j.isci.2026.116093

SUMMARY

Licorice-derived licochalcone A (LA) has antitumor effects, while conventional PTMC-coated biliary stents relieve malignant biliary obstruction but lack tumor-suppressive function and suffer from in-stent restenosis. This study fabricated an LA-loaded PTMC composite stent coating via favorable material compatibility for local sustained drug delivery. The coating improves surface hydrophobicity, enables stable LA release and good biocompatibility, and efficiently inhibits cholangiocarcinoma and colorectal cancer cell growth and tumor progression. LA exerts antitumor activity by regulating the CYP19A1-mediated GPR30-AKT pathway. This dual-functional coating offers a feasible strategy for clinical biliary stent modification and local tumor intervention.

INTRODUCTION

Licochalcone A (LA) (CAS no. 58749-22-7), molecular formula $C_{21}H_{22}O_4$, is a pharmacologically significant flavonoid primarily isolated from *Glycyrrhiza*.[1] LA is historically regarded as a by-product during glycyrrhizic acid extraction, but LA has witnessed substantial pharmacological advancements in recent years. It exhibits potent inhibitory effects on the proliferation of carcinoma (e.g., hepatocellular carcinoma, breast, and colon cancer).[2] Although extensive data indicate that the bioactivity of LA is mediated through diverse signaling pathways (e.g., PI3K/Akt/mTOR, MDM2, P53, p38, caspase-3-dependent apoptosis, and MAPK), its precise mechanism of action remains elusive.[3–6] Additionally, like other flavonoids/flavones, LA possesses suboptimal pharmacokinetic properties, including poor aqueous solubility, low bioavailability, limited permeability, and instability, despite favorable organic solubility.[7] These inherent weaknesses significantly restrict its widespread clinical implementation, underscoring an urgent need for sophisticated delivery strategies to harness its therapeutic potential while circumventing these limitations.

Malignant obstructive jaundice predominantly affects elderly patients and is commonly caused by primary liver cancer, cholangiocarcinoma, metastatic carcinoma, or pancreatic carcinoma compressing or invading the biliary tract.[8,9] Notably, colorectal cancer liver metastases (CRCLMs) represent another major cause of malignant biliary obstruction.[10] The liver is the predominant site of hematogenous metastasis in colorectal cancer, with 15%–25% of patients presenting with synchronous liver metastases at diagnosis and an additional 15%–25% developing metachronous metastases after curative resection of the primary tumor.[11] Critically, hilar or perihilar metastatic lesions can directly compress the common bile duct or hepatic ducts, leading to obstructive jaundice that is clinically indistinguishable from that caused by primary biliary malignancies and frequently necessitates biliary stenting.[11] This leads to biliary stenosis/obstruction, cholestasis, and markedly elevated serum bilirubin levels, resulting in severe hepatic dysfunction and related symptoms.[12,13] With rising incidence of biliary malignancies, the disease significantly impairs patients' physical and mental well-being and activities of daily living.[14] Clinically, biodegradable biliary stents have been increasingly used for the treatment of both malignant and benign biliary obstructions, and these stents can be further functionalized by loading therapeutic agents to enhance treatment efficacy.[15] Research demonstrates that percutaneous transhepatic biliary drainage (PTBD) combined with stent implantation effectively reduces total serum bilirubin, improves liver function, prolongs survival, minimizes perioperative tissue damage, and accelerates postoperative recovery, leading to its widespread international adoption.[16–18] While biliary stents offer

This is an open access article under the CC BY-NC-ND license (http://creativecommons.org/licenses/by-nc-nd/4.0/).

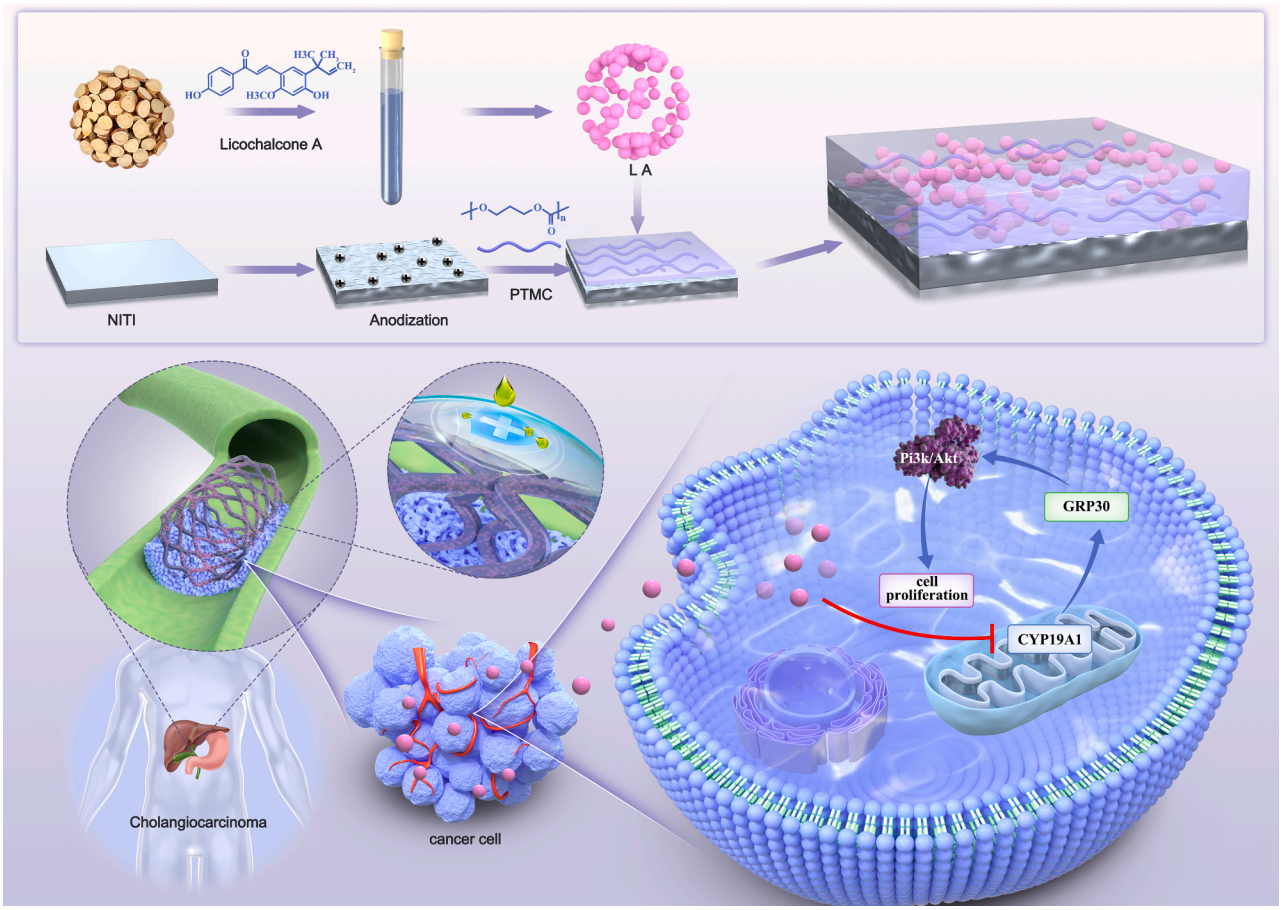

Figure 1. Schematic diagram illustrating the proposal of LA@PTMC coating construction and the mechanism by which it inhibits tumor cell proliferation via targeting CYP19A1 to suppress GPR30-mediated AKT signaling pathway as well as antifouling, which improved stent obstruction

advantages such as low reintervention rates and cost-effectiveness, their clinical utility is limited by complications including biliary sludge deposition, biofilm formation, and tumor ingrowth, which cause lumen obstruction, stent dysfunction, and reduced patency duration.[19–21] Addressing these limitations requires strategies to alleviate obstruction and extend stent patency.

Various synthetic coatings—encompassing organic, metallic, and inorganic formulations—have been engineered to prevent stent obstruction.[22–24] Nevertheless, these monolithic coatings demonstrate limited efficacy in satisfying the multifarious demands imposed by the harsh luminal microenvironment. For instance, while the polyvinyl benzyl chloride-D-glucaro-1,4-lactonate polymer (PVBC-DGL) coating effectively impedes biliary sludge deposition, it lacks additional bifunctionality.[25] Furthermore, our prior research developed a poly (trimethylene carbonate) (PTMC) blended with covalent organic frameworks (COFs) coating demonstrating antifouling properties; however, its deficiency in antitumor efficacy constrained clinical applicability.[26] Therefore, extending the functional longevity of these implants while concurrently enhancing their bioactivity presents a formidable challenge pivotal to advancing clinical translation.

Inspired by existing stent coating strategies, we selected PTMC, a biodegradable polymer with proven biocompatibility and film-forming ability, as a versatile matrix for sustained drug release. LA was chosen as the therapeutic agent to address tumor ingrowth. Building upon our previous work that established the robust antifouling properties of the PTMC platform, this study aims to functionalize this matrix with LA while verifying that the critical surface hydrophobicity required for antifouling protection is preserved. Specifically, we sought to evaluate whether this LA-integrated coating can simultaneously maintain the physicochemical basis for surface hydrophobicity and deliver potent localized antitumor activity. By combining antifouling surface properties with localized antitumor therapy in a unified coating, this work addresses the dual pathologies of stent failure, offering a promising proof-of-concept strategy with the potential to improve long-term patency in malignant biliary obstruction.

RESULTS

Assessment of LA@PTMC characteristic

An LA@PTMC nanocomposite coating was fabricated on a nickel&titanium (NITI) substrate, as schematically illustrated in

A

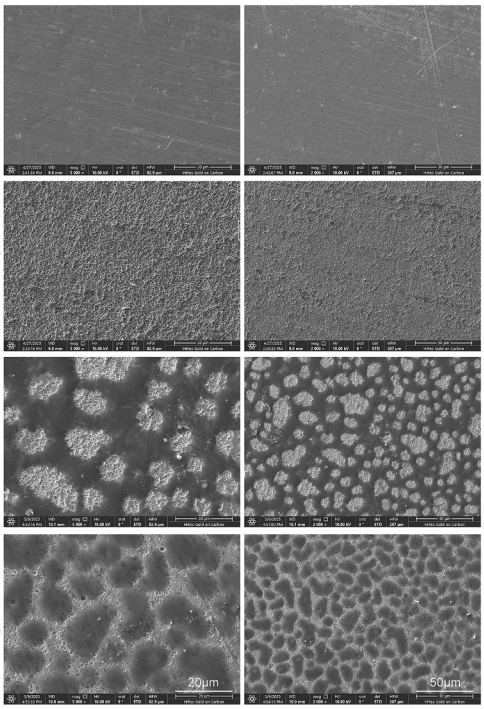

Element	Atomic %	Atomic % Error	Weight %	Weight % Error	Net Counts
C	26.3	0.1	7.5	0.0	188 156
O	1.2	0.2	0.5	0.1	7 639
Ti	36.2	0.1	41.3	0.1	2 906 480
Ni	36.3	0.1	50.8	0.1	1 685 602

Element	Atomic %	Atomic % Error	Weight %	Weight % Error	Net Counts
C	29.2	0.2	8.6	0.0	197 718
O	1.5	0.2	0.6	0.1	8 719
Ti	34.3	0.1	40.4	0.1	2 585 816
Ni	35.0	0.1	50.4	0.1	1 523 391

Element	Atomic %	Atomic % Error	Weight %	Weight % Error	Net Counts
C	39.9	0.2	14.1	0.1	396 485
O	7.4	0.2	3.5	0.1	59 148
Ti	26.5	0.1	37.3	0.1	2 782 476
Ni	26.1	0.1	45.1	0.1	1 579 767

Element	Atomic %	Atomic % Error	Weight %	Weight % Error	Net Counts
C	41.3	0.2	16.0	0.1	497 643
O	13.7	0.2	7.0	0.1	130 074
Ti	22.8	0.1	35.1	0.1	2 786 218
Ni	22.2	0.0	41.9	0.1	1 566 015

B

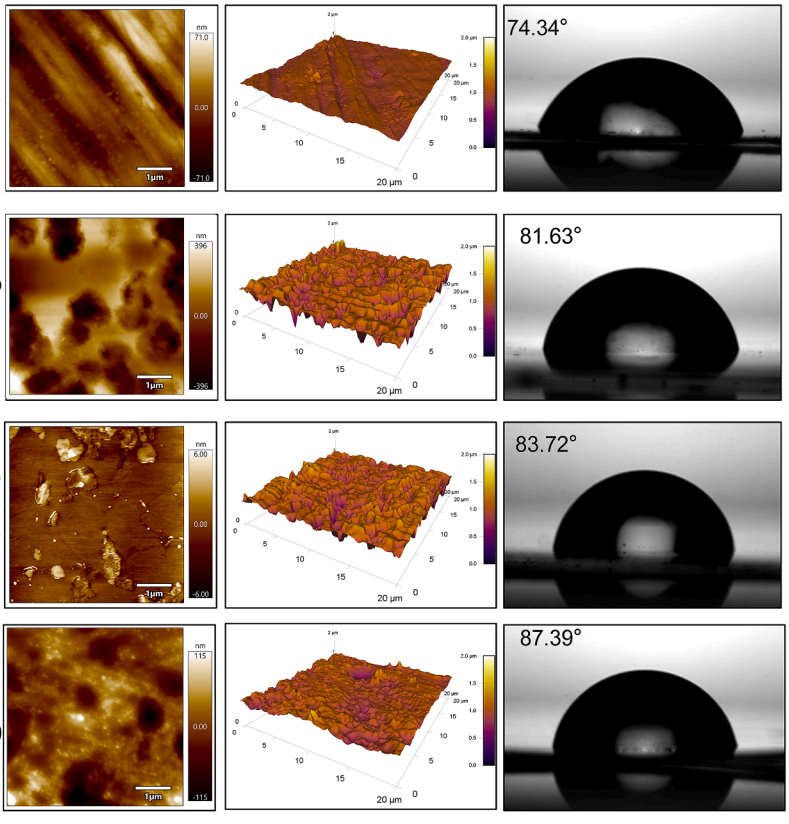

C

D

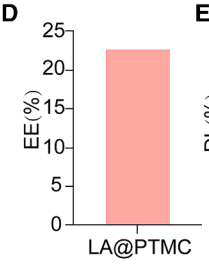

E

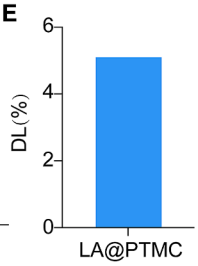

F

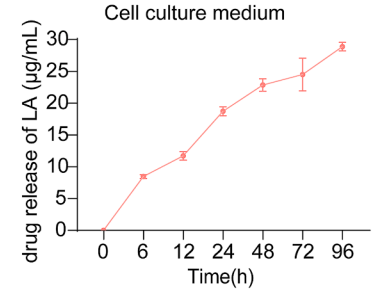

G

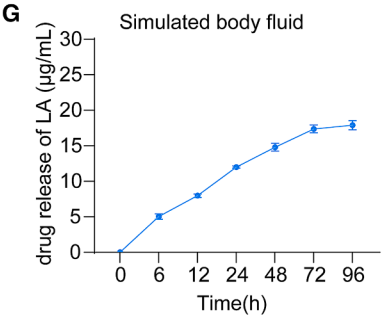

(legend on next page)

Figure 1. The NITI surface was first subjected to plasma electrolytic oxidation (PEO) anodization to confer a positive charge, facilitating adhesion with the negatively charged PTMC layer via electrostatic attraction. Subsequently, PTMC mixed with LA based on the physicochemical affinity principle (“like dissolves like”), was applied to the anodized surface to form the LA@PTMC composite. Examination of surface morphologies by scanning electron microscopy (SEM) (Figure 2A) revealed that the uncoated NITI substrate exhibited prominent scratches from mechanical polishing. PEO anodization produced a surface covered with dense, coarse particles, largely obscuring the scratches. Further coating with PTMC or LA@PTMC resulted in distinct island-like (PTMC) or honeycomb-like (LA@PTMC) polymer deposition patterns, with the LA@PTMC deposition appearing more uniform. Energy-dispersive X-ray spectroscopy (EDS) analysis confirmed successful coating: the atomic percentages of nickel (34%–36% ± 0.1%) and titanium (34%–36% ± 0.1%) in bare NITI and PEO-anodized surfaces were significantly higher than in the coated groups (22%–26% ± 0.1% for both elements), while carbon content—the major element in PTMC—increased dramatically, reaching 41.3% ± 0.2% for LA@PTMC and 39.9% ± 0.2% for PTMC, compared with 26.3% ± 0.1% (NITI) and 29.2% ± 0.2% (PEO). Furthermore, the oxygen content in LA@PTMC (13.7% ± 0.2%) exceeded that in PTMC (7.4% ± 0.2%), consistent with the higher oxygen content in LA’s chemical structure, confirming LA incorporation. Atomic force microscopy (AFM) analysis (Figure 2B) revealed that the LA@PTMC coating modulated surface roughness, exhibiting microscale elliptical prominences exceeding 2 μm in height, contrasting with the smoother profiles of bare NITI, PEO, and PTMC surfaces. Given the water solubility of biliary sludge, the coating’s interaction with water was evaluated. Water contact angle (CA) measurements (Figure 2C) demonstrated the inherent hydrophilicity of bare NITI (CA = 74.34°). The LA@PTMC coating significantly increased hydrophobicity (CA = 87.39°), with PEO (81.63°) and PTMC (83.72°) coatings also showing increased CA measurements, attributable to augmented surface roughness. Additionally, the LA@PTMC coating on the stent surface exhibited approximately 23% encapsulation efficiency (EE) and 5% drug loading (DL) (Figures 2D and 2E). Drug release kinetics from the LA@PTMC-coated stent were evaluated in both cell culture medium (Figure 2F) and simulated body fluid (SBF) (Figure 2G) over a 96 h period. LA was released in a sustained manner from the coating, with cumulative concentrations reaching approximately 28.8 μg/mL in cell culture medium and 17.9 μg/mL in SBF by 96 h. The result demonstrated a similar drug cumulative release curve with that of cell culture medium, but faster. We speculated that the protein adsorption within cell culture medium could affect drug release[27] Together, the release profile exhibited a gradual and sustained pattern, indicating that the LA@PTMC coating is capable of enabling prolonged local delivery of LA under conditions that mimic physiological environments. Collectively, these results indicate that the LA@PTMC coating enhances surface hydrophobicity to resist biliary sludge deposition while enabling the sustained release of LA.

LA@PTMC inhibited cholangiocarcinoma growth by regulating PI3K-AKT signaling pathway *in vivo*

Based on the aforementioned findings, this study evaluated the antitumor efficacy of the LA@PTMC coating *in vivo*. Tumors, along with either PTMC or LA@PTMC implants, were introduced into nude mice. No measurements were taken during the first 7 days post-implantation to allow for initial tumor growth. Starting from day 7, body weight and tumor diameter of each mouse were measured every 3 days for a total duration of 24 days. The total duration of mouse housing throughout the entire experiment was 31 days (encompassing the initial 7-day tumor growth phase and the subsequent 24-day treatment/measurement phase). As shown in Figure 3A, tumor volumes in the LA@PTMC and LA (intragastric [i.g.]) groups were significantly lower than in the control group from day 10 onward, whereas PTMC alone showed no significant difference. Furthermore, the antitumor effect of LA@PTMC was superior to that of LA (i.g.). Correspondingly, the tumor weights and sizes in the LA@PTMC and LA (i.g.) groups were significantly smaller and lighter than those in the control group, with LA@PTMC demonstrating greater efficacy (Figures 3B and 3C). Notably, mouse body weights showed no significant differences among the control, LA@PTMC, and PTMC groups; however, the LA (i.g.) group exhibited a stably lower body weight compared with the control from day 7 to the endpoint (Figure 3D). Histopathological analysis (H&E staining) revealed that both LA@PTMC and LA (i.g.) induced loosening of the tumor structure compared with the control groups (Figure 3E). Most importantly, Ki67 staining (a biomarker of cell proliferation) demonstrated significantly less staining in the LA@PTMC and LA (i.g.) groups compared with the control, while PTMC alone showed no effect; notably, LA@PTMC exhibited even less Ki67 staining than LA (i.g.) (Figure 3F). These results demonstrate that LA@PTMC effectively inhibited RBE tumor growth, outperforming LA (i.g.), while avoiding the body weight decrease associated with the side effects of oral LA. Next, the potential pharmacological mechanism of LA@PTMC was investigated via RNA sequencing (RNA-seq).

Figure 2. Characterization of surface morphology and properties of different materials

(A) Scanning electron microscopy (SEM) images of NITI, anodizing PEO, PTMC, and LA@PTMC. The tables below SEM image display the elemental composition and weight percentages of different materials. Scale bars, 20 μm or 50 μm.

(B) Atomic force microscopy (AFM) images and 3D surface topography of NITI, anodizing PEO, PTMC, and LA@PTMC.

(C) Water contact angle measurements of NITI, anodizing PEO, PTMC, and LA@PTMC.

(D and E) Encapsulation efficiency (EE) and (E) drug loading (DL) efficiency of LA@PTMC.

(F) Drug release profile of LA in cell culture medium over time.

(G) Drug release profile of LA in simulated body fluid over time.

The comparisons among multiple groups were carried out using a parametric one-way ANOVA test, based on the normality results. Data are represented as mean ± SEM.

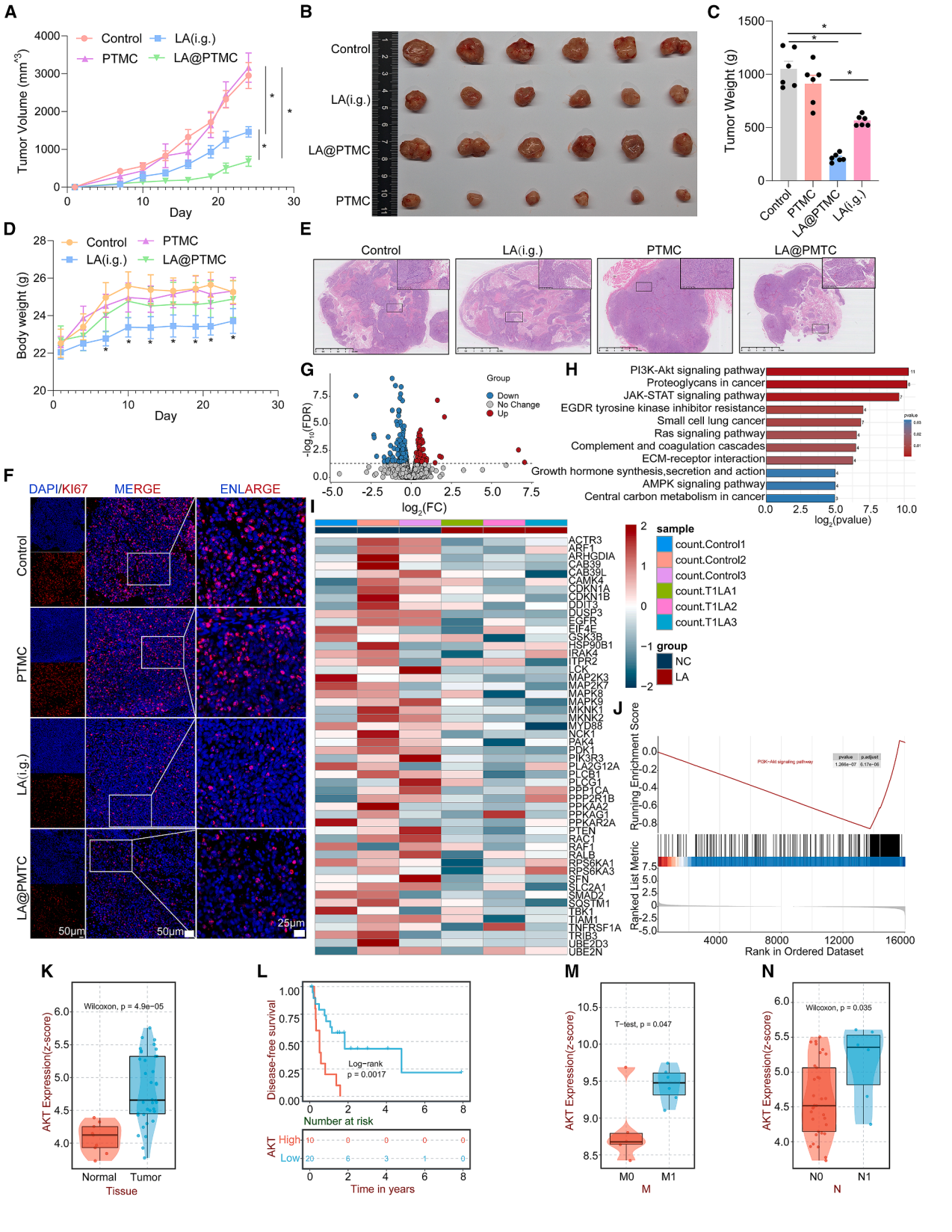

(legend on next page)

Screening and analysis of differentially expressed genes (DEGs) and Kyoto Encyclopedia of Genes and Genomes (KEGG) pathways identified the PI3K-AKT signaling pathway as the top enriched pathway (Figures 3G and 3H). A heatmap further validated that LA@PTMC downregulated the expression of most genes associated with this pathway (Figure 3I). Gene set enrichment analysis (GSEA) confirmed a significant negative correlation between the PI3K-AKT pathway and the LA@PTMC treatment group (Figure 3J). Bioinformatics analysis of AKT (a key effector of the PI3K-AKT pathway) revealed its higher expression in cholangiocarcinoma tumor tissue compared with normal tissue (Figure 3K), as well as a negative correlation with disease-free survival (DFS) (Figure 3L). Additionally, AKT expression was elevated in patients with advanced stages of cholangiocarcinoma. These results collectively demonstrate that LA@PTMC inhibits tumor growth by regulating the PI3K-AKT pathway and underscore its application value, particularly as this target pathway is predominant in severe cholangiocarcinoma patients who are prone to malignant obstructive jaundice.

LA@PTMC inhibited cancer progress by inhibiting cell proliferation via PI3K-AKT signaling pathway

Building on the PI3K-AKT pathway findings, we next investigated the specific antitumor effects of LA@PTMC. Given the role of PI3K-AKT as a classic cancer-promoting pathway, HCT116 colon cancer cells were included as an additional *in vitro* model. Concentration optimization revealed that 6 μM or 12.5 μM LA partially or completely inhibited HCT116 proliferation, while 12 μM or 25 μM LA exerted similar effects on RBE cells (Figures 4A, 4C, and S1A). Consequently, 6 μM (HCT116) and 12 μM (RBE) LA were selected as drug controls. LA@PTMC (but not PTMC alone) significantly inhibited growth in both cell lines (Figures 4B, 4D, and S1A). Clonogenic assays—designed to simulate single-cell deposition on stent surfaces—demonstrated that LA@PTMC completely suppressed colony formation, exhibiting efficacy comparable to 12.5 μM/25 μM LA and superior to lower concentrations (6 μM for HCT116; 12 μM for RBE) (Figures 4E–4J). Cell cycle analysis showed that 6 μM (HCT116) and 12 μM (RBE) LA blocked S-to-G2/M phase transition (Figures 4K–4N), an effect replicated by LA@PTMC (Figures 4O–4R). Further functional assays revealed no obvious cytotoxic effect (LDH release: 2%–6% for LA@PTMC or 25 μM LA; Figures 4S–4U) and no impact on tumor cell migration (Figures S1B and S1C). These results demonstrate that LA@PTMC inhibits tumor proliferation primarily through cell-cycle arrest. Given PI3K-AKT's established role in cell cycle progression, these findings corroborate pathway involvement.[28] Immunohistochemistry (IHC) confirmed significantly reduced AKT expression in LA@PTMC- and LA (i.g.)-treated tumor tissues versus controls, with LA@PTMC showing greater suppression than LA (i.g.) (Figure 5A). *In vitro*, both LA@PTMC and LA (across concentrations) downregulated AKT protein expression in HCT116 and RBE cells, while PTMC had no effect (Figures 5B–5I). Notably, LA and LA@PTMC also suppressed AKT mRNA levels in both cell lines (Figures 5J and 5K), suggesting LA may indirectly regulate PI3K-AKT signaling indirectly.

CYP19A1 was the target of LA from LA@PTMC

Building on prior findings, we identified potential candidates as the putative target of LA within the LA@PTMC coating. SwissTargetPrediction analysis nominated CYP19A1 as the top candidate targets (Figure 6A). Molecular docking (MD) confirmed strong binding affinity between LA and human CYP19A1 (binding energy: −5.22 kcal/mol, belonging to strong binding[29]; binding site: GLN-141; Figure 6B), further validated by microscale thermophoresis (MST) revealing a dissociation constant (KD) of 7.7809 μM (Figure 6C). To further validate the direct binding interaction between LA and CYP19A1 in RBE cells, we performed a cellular thermal shift assay (CETSA). The binding interaction between CYP19A1 and LA was further investigated using CETSA to assess thermal stability changes in RBE cells. CETSA results revealed that LA treatment significantly enhanced CYP19A1 thermal stability, with pronounced effects observed between 53°C and 65°C. (Figures 6D and 6E). The Cancer Genome Atlas (TCGA) data demonstrated elevated CYP19A1 expression in cholangiocarcinoma and multiple other tumors versus normal tissues (Figure 6F), correlating with poor disease-free survival (DFS; Figure 6J) and advanced tumor stages (Figures 6G–6I). As such, *in vitro* studies showed decreased CYP19A1 protein expression following LA@PTMC and free LA treatments versus controls (Figures 6K–6R), and *in vivo* analysis of tumor tissues also revealed significant suppression of CYP19A1 in LA@PTMC- and LA (i.g.)-treated groups, with LA@PTMC exhibiting stronger inhibition than LA (i.g.) (Figure 6S). These results establish CYP19A1 as a functional target mediating LA@PTMC's antitumor effects.

Figure 3. LA@PTMC inhibited cholangiocarcinoma growth

(A) Tumor volume of tumor-bearing mice under different treatments over time (n = 6).
(B) Photographs of tumors dissected from mice under different treatments.
(C) Weight of tumors dissected from mice of different treatments (n = 6).
(D) Weight of tumor-bearing mice under different treatments over time (n = 6).
(E) H&E staining of tumors tissue.
(F) Representative immunofluorescence images of KI67 in tumor tissues among all groups. Scale bars, 50 μm.
(G) RNA-seq was performed between control and LA@PTMC tumor tissue and DEGs were showed as volcano picture.
(H) The KEGG pathway was analyzed.
(I and J) The GSEA of PI3k-AKT and heatmap was visualized.
(K)The AKT expression at normal and tumor tissue with cholangiocarcinoma was shown.
(L) The disease-free survival (DFS) was shown between AKT high expression and AKT low expression of patient with cholangiocarcinoma. The AKT expression on different tumor stages of cholangiocarcinoma was shown (M for metastasis and N for lymphatic).
The comparisons among multiple groups were carried out using a parametric one-way ANOVA test, based on the normality results. Data are represented as mean ± SEM. *$p < 0.05$.

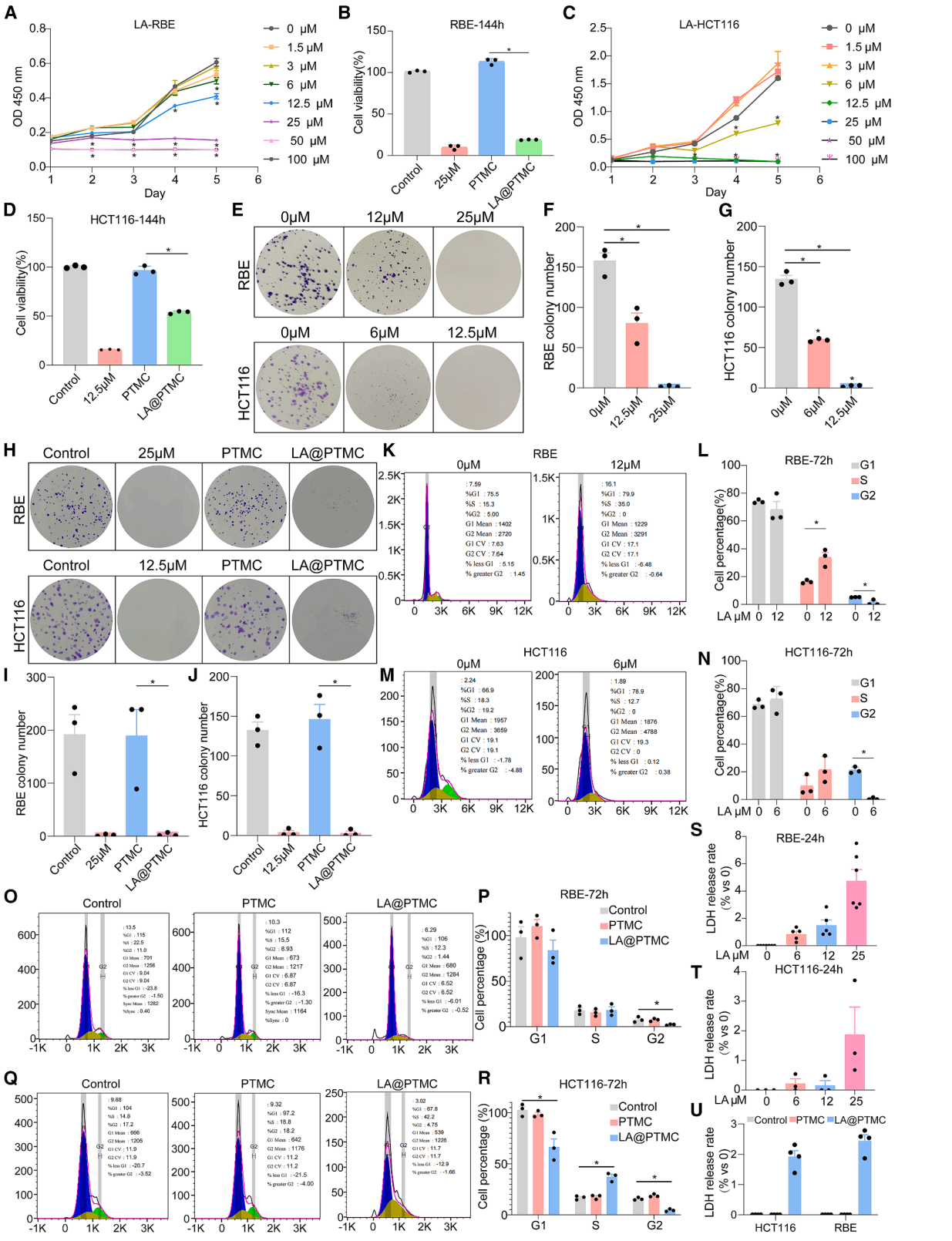

(legend on next page)

LA@PTMC target CYP19A1 to inhibit GPR30 induce PI3K-AKT signaling pathway

Given reported crosstalk between CYP19A1 and the GPR30-PI3K-AKT axis, we investigated this pathway.[30] *In vitro*, LA@PTMC and free LA downregulated GPR30 protein expression (Figures 7A–7H) and mRNA expression (Figures 7I and 7J) in tumor cells. Bioinformatics analysis confirmed GPR30's negative correlation with DFS and elevated expression in advanced-stage cholangiocarcinoma (Figures 7K–7M), aligning with CYP19A1 and AKT profiles. Critically, *in vivo* analysis showed enhanced GPR30 suppression by LA@PTMC versus all other groups (Figure 7N), demonstrating that LA@PTMC inhibits tumor growth by disrupting the CYP19A1-GPR30-PI3K-AKT signaling cascade.

LA@PTMC compatibility study *in vivo*

Biocompatibility assessment revealed no significant differences in serum biomarkers (ALT, AST, TP, serum albumin [ALB], globulin-GLOB, BUN; Figures 8A–8C), hematological parameters (WBC, RBC, platelets, hemoglobin; Figures 8D–8F), or organ weights (liver, heart, lung, spleen, kidney; Figures 8G–8K) across control, PTMC, LA@PTMC, and LA (i.g.) groups. Histopathological evaluation (H&E staining) confirmed normal tissue architecture in all major organs (Figure 8L), affirming the clinical safety profile of the LA@PTMC stent.

DISCUSSION

The development of the LA@PTMC-coated stent represents a strategic approach to addressing the dual-pathology nature of biliary stent failure: mechanical occlusion by biliary sludge and biological obstruction due to neoplastic ingrowth. A critical requirement for clinical translation is the use of PTMC as a stable, biocompatible matrix that maintains its structural and functional integrity under the harsh, dynamic conditions of the biliary tract, which is characterized by bile salts, phospholipids, enzymes, and electrolytes. Extensive studies have demonstrated that PTMC undergoes uniform surface erosion without bulk degradation, preserving coating morphology while generating neutral byproducts that mitigate local corrosion.[31] Our prior studies further confirmed that PTMC demonstrates outstanding corrosion resistance and antifouling properties in both rabbit bile ducts and an *in vitro* bile flow simulation system.[26] In the LA@PTMC system, PTMC functions as the foundational matrix, and its inherent stability is anticipated to maintain the coating's critical physicochemical properties throughout the stent's intended functional lifespan, thereby ensuring durable resistance to biliary sludge adhesion. Our water CA measurements demonstrated that both PTMC and LA@PTMC coatings exhibit pronounced hydrophobicity—a critical property to generate a non-adhesive surface that physicochemically repels bacteria and calcium bilirubinate precursors, which are key initiators of biliary sludge formation.[32,33] Moreover, PTMC's surface-eroding profile enables sustained, homogeneous drug release; for instance, paclitaxel-loaded PTMC showed only ~30% cumulative release over 20 days,[34] supporting its suitability as a long-acting carrier for localized delivery of LA. This favorable release kinetics underscores our rationale for selecting PTMC as the primary carrier for localized, long-acting delivery of LA.

LA's antitumor potential has been overshadowed by its rapid metabolic clearance and negligible oral bioavailability, rendering it a clinically marginalized compound. By anchoring LA within the PTMC stent coating, we circumvent first-pass metabolism and systemic degradation, enabling direct, sustained exposure to the neoplastic epithelium. This spatial targeting strategy mirrors the success of vascular drug-eluting stents (e.g., everolimus-eluting stent) but innovates by repurposing a natural product with limited clinical utility.[35] The superior tumor suppression by LA@PTMC over LA (i.g.) *in vivo* validates this approach, demonstrating how biomaterial engineering can rescue compounds with promising pharmacology yet pharmaceutically challenging compounds.

It is important to emphasize that the primary innovation of this work lies not in the discovery of LA antitumor activity, which has been reported in various cancer models,[36] but in its rational integration into a locally drug-eluting biliary stent platform. By leveraging the PTMC coating as a sustained-release reservoir, we overcome LA's well-documented pharmacokinetic limitations and achieve high local concentrations directly at the stent-tumor interface. The *in vitro* mechanistic studies presented here are, therefore, intended to provide a plausible biological context for the superior *in vivo* efficacy of the LA@PTMC stent, rather than to establish novel molecular pathways. Central to this antitumor efficacy is the targeted disruption of the CYP19A1-GPR30-AKT signaling cascade by locally released LA, a pathway increasingly implicated in hormone-sensitive malignancies including cholangiocarcinoma. Notably, this molecular axis is not exclusive to biliary cancers; emerging evidence confirms its functional relevance in colorectal carcinoma as well. Specifically, Liu et al. identified CYP19A1 as a prognosis-related gene in colon cancer that drives tumor progression through local estrogen synthesis, subsequent activation of the GPR30-AKT pathway, and upregulation of pro-inflammatory cytokines, including IL-6 and TGF-β.[30] Our dual-cell validation using both RBE (cholangiocarcinoma) and HCT116 (colorectal carcinoma) thus reflects a clinically grounded strategy: while RBE models primary malignant biliary obstruction, HCT116 represents secondary obstruction caused by CRCLMs, a frequent indication for palliative stenting due to hilar metastatic compression. Targeted therapies against specific genetic alterations, such as FGFR2 fusions or IDH1 mutations, represent the current standard for treating biliary tract cancers[37]]. However, a significant

Figure 4. LA@PTMC inhibited cell proliferation by inhibiting cell cycle

RBE (A and B) or HCT116 (C and D) cells were treated with various concentrations of LA for 5 days and CCK8 assay was carried out to detect cell growth ($n = 3$). The RBE and HCT116 cells were cloned by treating with various concentration of LA for 10 days (E–G) as well as LA@PTMC and PTMC ($n = 3$) (H–J). Cell cycle of HCT116 and RBE was detected by FC after treating with various concentrations of LA, LA@PTMC, or PTMC for 72 h ($n = 3$) (K–R). The LDH release assay was carried out after cells were treated with various concentrations of LA, PTMC, or LA@PTMC for 24 h ($n \geq 3$) (S–U). The comparisons among multiple groups were carried out using a parametric one-way ANOVA test, based on the normality results. Data are represented as mean ± SEM. $^*p < 0.05$.

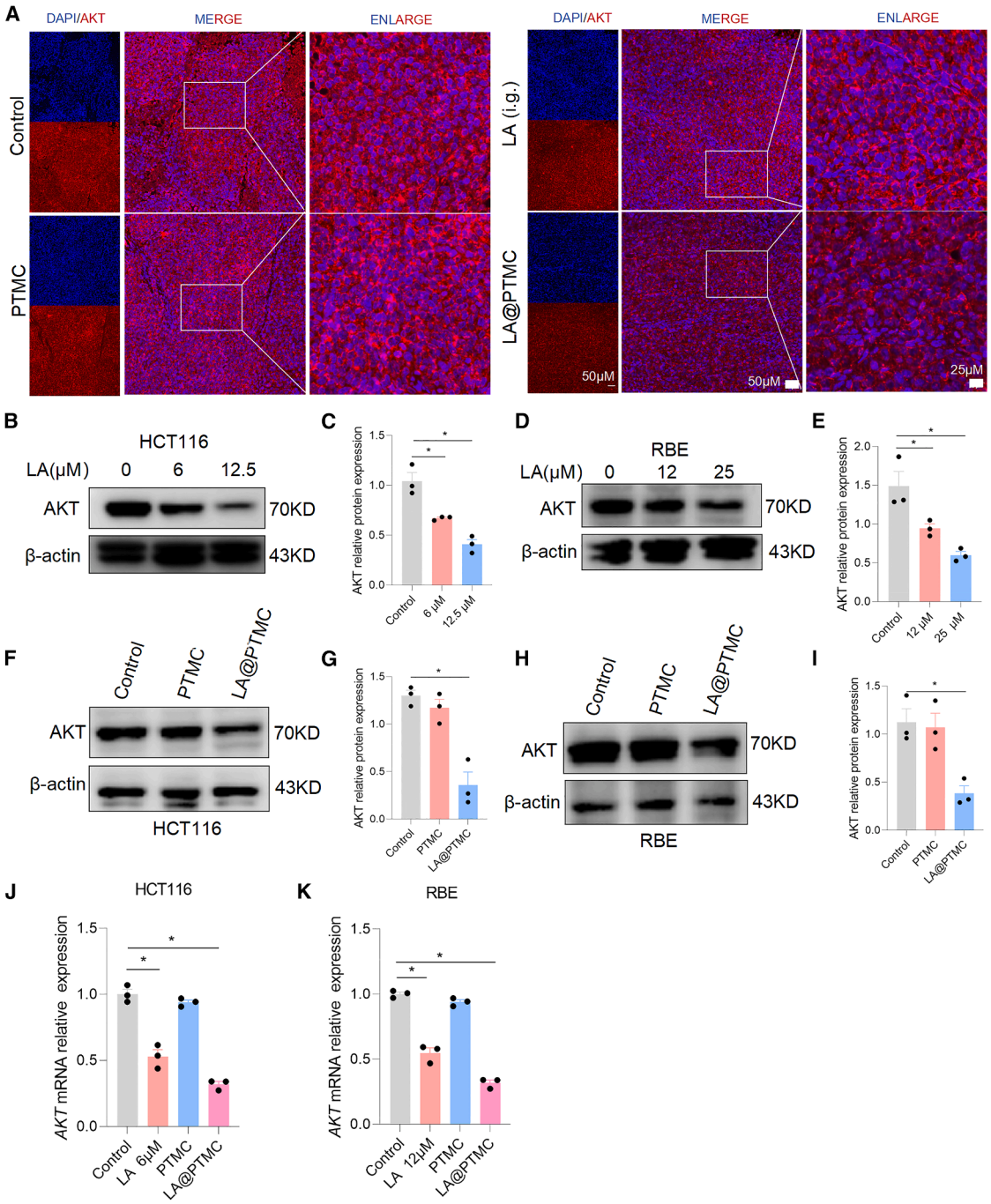

Figure 5. LA@PTMC inhibited AKT expression

(A) Representative IF images of AKT in tumor tissues among all groups. Scale bars, 50 μm.

(B and C) The protein expression level of AKT determined by western blot (WB) in HCT116 after treatment with different concentrations of LA (n = 3).

(D and E) The protein expression level of AKT determined by WB in RBE after treatment with different concentrations of LA (n = 3).

(F and G) The protein expression level of AKT determined by WB in HCT116 after treatment with LA@PTMC or PTMC (n = 3).

(H and I) The protein expression level of AKT determined by WB in RBE after treatment with LA@PTMC or PTMC (n = 3).

(J and K) The mRNA levels of AKT determined by RT-PCR in HCT116 (J) and RBE (K) after treatment with LA@PTMC, LA, or PTMC for 72 h.

The comparisons among multiple groups were carried out using a parametric one-way ANOVA test, based on the normality results. Data are represented as mean ± SEM. *$p < 0.05$.

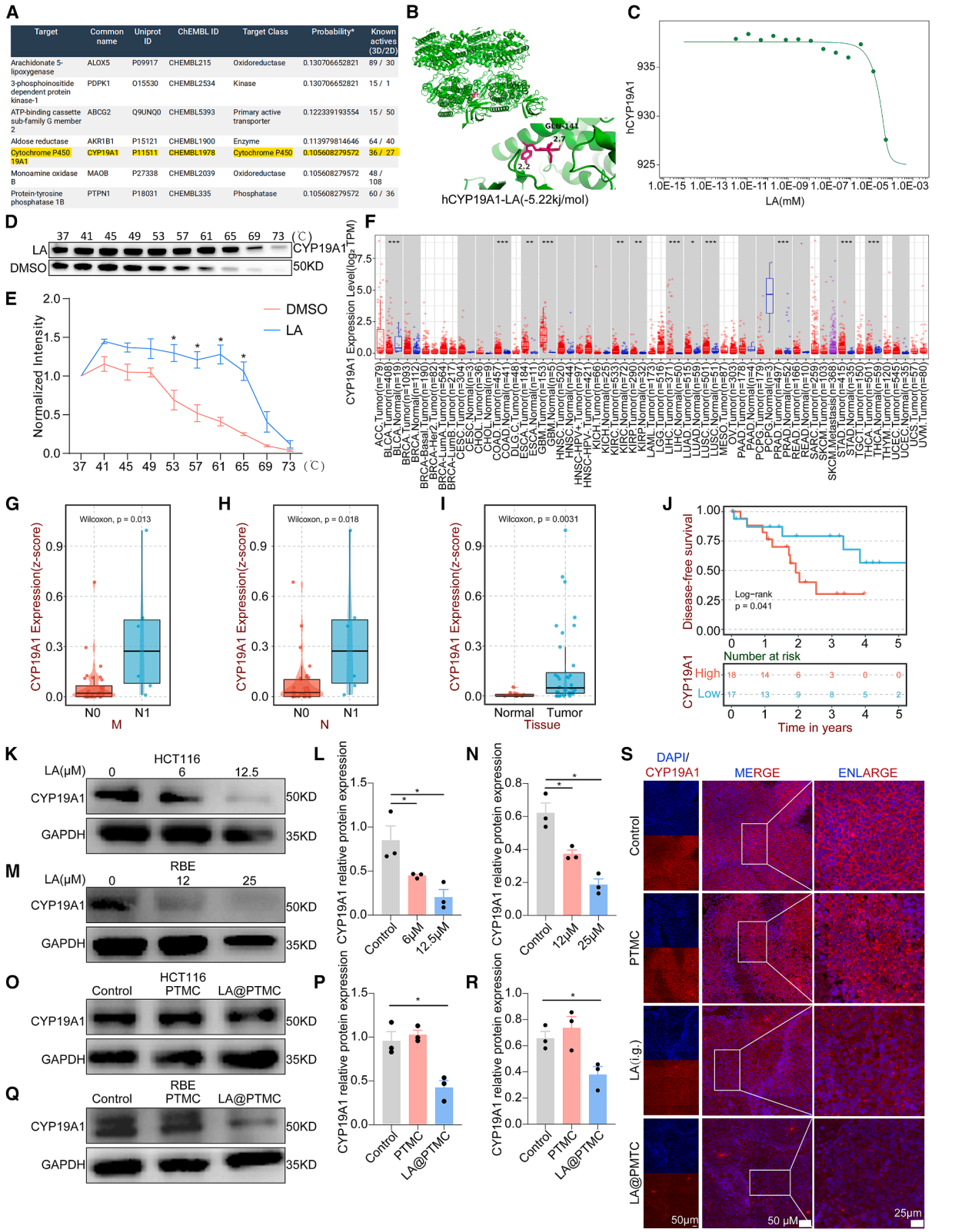

(legend on next page)

proportion of patients lack these actionable mutations, underscoring the need to identify alternative therapeutic targets. Emerging evidence highlights the role of estrogen signaling in biliary carcinogenesis. Studies indicate that CYP19A1 and its downstream receptor GPR30 are frequently upregulated in estrogen-sensitive malignancies, including biliary cancer.[38,39] This axis promotes tumor progression by activating key oncogenic pathways, including well-known EGFR/MAPK and PI3K/AKT.[40] Our study demonstrates that LA directly suppresses both CYP19A1 and GPR30 expression. Given that CYP19A1 catalyzes the rate-limiting step in estrogen biosynthesis,[41] its inhibition by LA may disrupt estrogen production and potentially affect subsequent GPR30-AKT mediated signaling. These findings suggest that LA exerts its antitumor effects, at least in part, through the modulation of the CYP19A1-GPR30-AKT signaling axis. While LA has been reported to possess auxiliary anti-inflammatory properties,[2,42] our findings supported by direct binding validation (e.g., CETSA) and coherent suppression of this signaling cascade, strongly suggest that its primary mechanism of action in biliary cancer is specific to regulate CYP19A1. Although, the inflammation is obviously relative to tumor progress, LA as an anti-inflammatory agent could play an anti-tumor role by immunoregulation in theory, which needs to be studied in future. Together, our results propose that LA-mediated modulation of this axis may contribute to tumor stasis through AKT-associated cell-cycle arrest and restoration of apoptosis, offering a potential therapeutic strategy by possibly targeting a pathway highly relevant to hormone-driven malignancies without relying on broad cytotoxic effects. This level of mechanistic focus, while not claiming novelty in the AKT pathway itself, aligns with contemporary paradigms in precision oncology by exploiting a defined molecular vulnerability that appears to be targeted in peri-stent neoplastic tissue.[43]

Our data consistently link LA treatment to the concomitant downregulation of CYP19A1 and AKT across multiple assays, including MD, MST binding, and western blot. In addition, TCGA analysis further shows that elevated CYP19A1 expression in human cholangiocarcinoma is associated with poor prognosis, serving to establish clinical relevance rather than causal mechanism. It is important to note that these observations represent associative evidence. The functional necessity of the CYP19A1-GPR30-AKT axis in mediating LA antitumor effect was not definitively proven in this study. Although, the temporal correlation between LA-induced suppression of upstream CYP19A1 and downstream inhibition of AKT and tumor growth in both RBE and HCT116 models strongly supports this mechanistic hypothesis, direct genetic validation (e.g., CYP19A1 or GPR30 knockdown/overexpression) would be required to conclusively establish causality in future.

While our study demonstrates the integrated efficacy of the LA@PTMC stent, we acknowledge that a precise quantitative pharmacokinetic/pharmacodynamic (PK/PD) relationship between local LA release and its distinct functional outcomes remains to be fully elucidated. We propose a conceptual framework based on our data: the sustained, low-level release of LA from the PTMC matrix is designed to maintain a local concentration above the minimum effective threshold for inhibiting the CYP19A1-GPR30-AKT axis in adjacent tumor cells, an effect that is supported by our binding and signaling data, suggesting a concentration-dependent relationship. In contrast, the resistance to sludge deposition is primarily attributed to the persistent hydrophobicity of the PTMC matrix itself. The role of LA here may be synergistic and indirect. Establishing this detailed PK/PD linkage is a critical next step to quantify the relationship between local LA concentrations over time and its specific biological effects. Such a model would not only deepen mechanistic understanding but also rationally guide the optimization of drug loading and release kinetics for clinical translation. Addressing these PK/PD parameters, specifically, the physiological release kinetics, local drug concentration, and compound stability is, therefore, a critical prerequisite for the clinical translation of the LA@PTMC stent.

This study presents a proof-of-concept for a bifunctional LA@PTMC coating strategy aimed at mitigating biliary restenosis. The coating design synergizes the hydrophobic antifouling properties of PTMC against sludge with the localized antitumor efficacy of LA. Crucially, our data indicate that stent-based delivery can potentially overcome LA's systemic limitations, such as low bioavailability and rapid degradation, demonstrating enhanced tumor suppression in preclinical models compared to oral administration. Mechanistically, our findings suggest that sustained LA release inhibits tumor growth by suppressing the CYP19A1-GPR30-AKT pathway. While further validation in orthotopic biliary models and long-term patency studies are required to confirm clinical translatability, this bifunctional platform provides a promising rationale for the future development of advanced interventional tools to maintain biliary patency in malignant obstruction.

Figure 6. CYP19A1 was the target of LA from LA@PTMC

(A) The potential target of LA was screened for SwissTargetPrediction database.

(B) MD analysis was carried out for LA binding hCYP19A1.

(C) MST was used to detect KD for LA binding of hCYP19A1, and KD was detected.

(D and E) CETSA demonstrated specific binding of LA to the CYP19A1 protein and statistical graph of CETSA (n = 3).

(F) The CYP19A1 expression on all cancer cells was analyzed by TCGA. The CYP19A1 expression at normal and tumor tissue with cholangiocarcinoma was shown.

(G–J). The CYP19A1 expression on different tumor stages of cholangiocarcinoma was shown (H for metastasis and I for lymphatic). DFS was shown between CYP19A1 high expression and low expression of patient with cholangiocarcinoma (J).

(K–N) The protein expression level of CYP19A1 determined by western blot (WB) in HCT116 or RBE after treatment with different concentrations of LA (n = 3).

(O–R) The protein expression level of CYP19A1 determined by WB in HCT116 or RBE after treatment with LA@PTMC or PTMC (n = 3).

(S) Representative immunofluorescence images of CYP19A1 in tumor tissues among all groups. Scale bars, 50 μm.

The comparisons among multiple groups were carried out using a parametric one-way ANOVA test, based on the normality results. Data are represented as mean ± SEM. *$p < 0.05$.

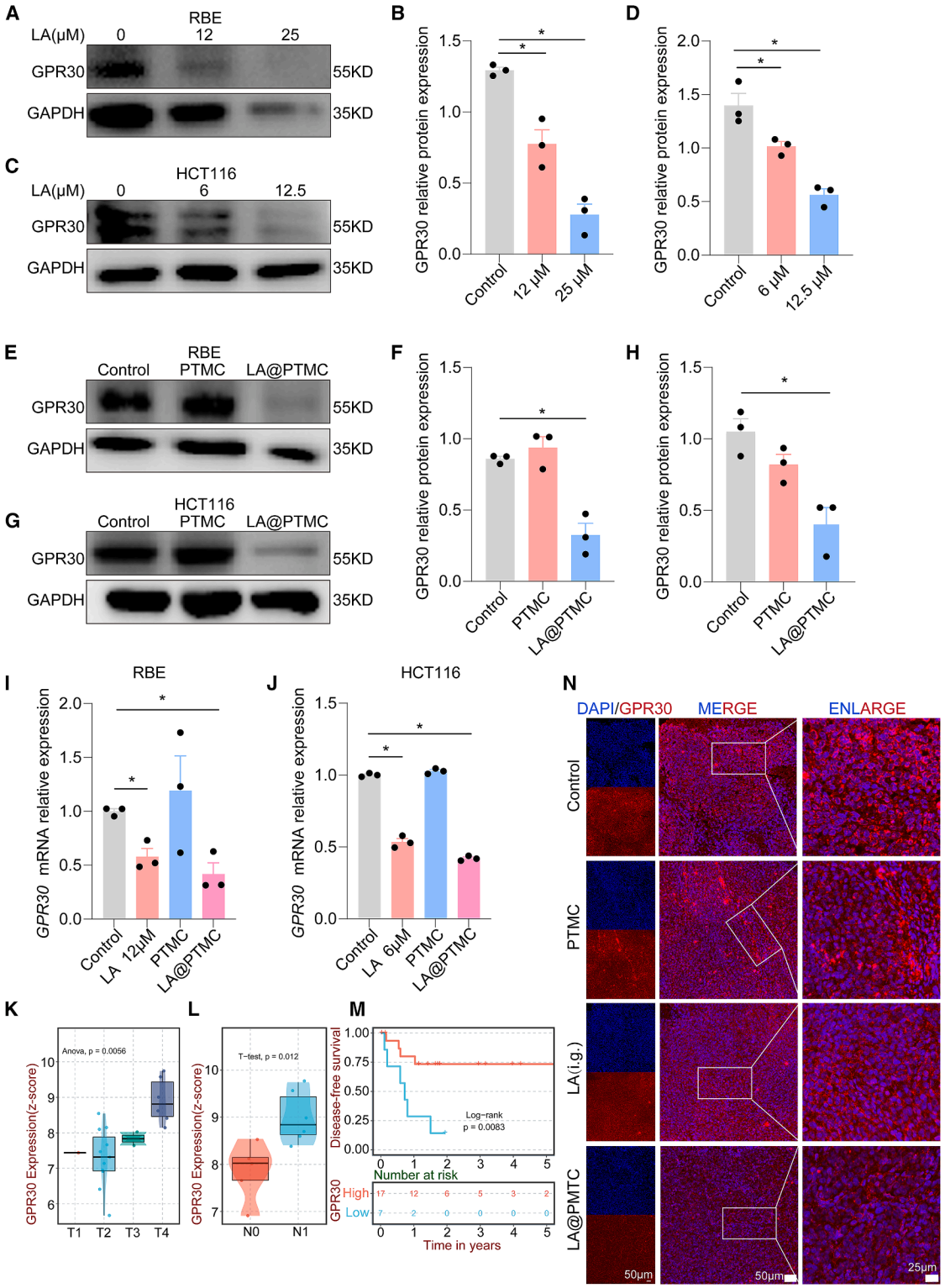

Figure 7. LA@PTMC inhibited the PI3K-AKT signaling pathway through inhibiting GPR30 expression

(A and B) The protein expression level of GPR30 determined by western blot (WB) in RBE after treatment with different concentrations of LA (n = 3).

(C and D) The protein expression level of GPR30 determined by WB in HCT116 after treatment with different concentrations of LA (n = 3).

(E and F) The protein expression level of GPR30 determined by WB in RBE after treatment with LA@PTMC or PTMC (n = 3).

(legend continued on next page)

Limitations of the study

Several key questions warrant further investigation to fully realize the clinical potential of this platform. First, while our data correlate CYP19A1 downregulation with anti-tumor efficacy, direct genetic validation—such as CYP19A1 or GPR30 knockdown and overexpression in patient-derived cholangiocarcinoma models—is needed to establish causal necessity of this axis. Second, long-term *in vivo* studies are required to comprehensively assess the biocompatibility of degrading PTMC and the durability of its anti-fouling performance under chronic biliary exposure. Finally, given the hormone-dependent nature of the targeted pathway, the influence of patient-specific factors (e.g., hormonal status, sex, and CYP19A1 expression heterogeneity) on therapeutic response must be systematically evaluated. A major concern for any drug-eluting device in the biliary system is the potential for off-target toxicity to the surrounding non-tumoral biliary epithelium, which could lead to inflammation, ulceration, or secondary strictures. Future studies utilizing large-animal models of biliary obstruction are imperative to rigorously assess the histological integrity of adjacent normal bile ducts, monitor markers of cholangitis, and determine the long-term safety of this platform.

RESOURCE AVAILABILITY

Lead contact

Further information and requests for resources and reagents should be directed to and will be fulfilled by the lead contact, Rui Zan (zanr@ywfudan.cn).

Materials availability

LA@PTMC coating generated in this study will be made available on request, but we may require a payment and/or a completed materials transfer agreement if there is potential for commercial application.

Data and code availability

- All data generated or analyzed during this study are included in this article (and its supplemental information). The raw data of all sequence in this study can be downloaded at https://www.biosino.org/node/home (accession no. OEP00006442).
- This paper does not report original code.
- Any additional information required to reanalyze the data reported in this paper is available from the lead contact upon request.
- Raw data were deposited on Mendeley at https://doi.org/10.17632/9vx86938md.1.

ETHICS APPROVAL STATEMENT

All animal experiments were approved by the Zhejiang Chinese Medical University Animal Ethical and Welfare Committee (Approval No. IACUC-20240909-09).

PATIENT CONSENT STATEMENT

No clinical trial was performed in the study.

CLINICAL TRIAL REGISTRATION

No clinical trial was performed in the study.

ACKNOWLEDGMENTS

This research was supported by grants from the National Natural Science Foundation of China (82304761 and 82374110). Chinese funding program for postdoctoral researcher (GZC20231701). and Natural Science Foundation of Zhejiang Province (LQN25H280006 and LY23H280005). Zhejiang Province Traditional Chinese Medicine Science and Technology Project (2025ZR017). The Science and Technology Department of the State Administration of Traditional Chinese Medicine, and the Zhejiang Provincial Administration of Traditional Chinese Medicine jointly built technology plan projects (GZY-ZJ-KJ-24065).

AUTHOR CONTRIBUTIONS

R.Z., L.Z., and L.Y. designed and supervised this project; L.J., Y.W., and J.X. performed most of the experiments; L.J., Y.W., Q.M., and B.F. analyzed the results; L.J., Y.L., and Y.Z. carried out bioinformatics analyses; Z.W., L.J., L.L., X.G., and X.W. contributed to the conception of schematic representation in figures; L.J. wrote the article with comments from all authors. All authors have read and approved the final manuscript.

DECLARATION OF INTERESTS

The authors declare no competing interests.

STAR★METHODS

Detailed methods are provided in the online version of this paper and include the following:

- KEY RESOURCES TABLE
- EXPERIMENTAL MODEL AND STUDY PARTICIPANT DETAILS
  - Cell culture
  - Animal experiments
- METHOD DETAILS
  - LA@PTMC preparation
  - Water contact angle test
  - Encapsulation efficiency and drug loading of LA on NITI
  - Drug release study of LA
  - Cell proliferation assay
  - Bioinformatics database analysis
  - Lactate dehydrogenase (LDH) release assay
  - Clone formation assay
  - RNA-seq analysis
  - Cell scratching test
  - Cell cycle by flow cytometry (FC) analysis
  - Safety evaluation *in vivo*
  - Immunofluorescence (IF) staining
  - Real-time quantitative polymerase chain reaction (RT-qPCR)
  - Hematoxylin and eosin (H&E) staining
  - Western Blot (WB)
  - Cellular thermal shift assay (CETSA)
  - Microscale Thermophoresis (MST) analysis

(G–M) The protein expression level of GPR30 determined by WB in HCT116 after treatment with LA@PTMC or PTMC ($n = 3$). The mRNA levels of GPR30 by RT-PCR in RBE (I) and HCT116 (J) after treatment with LA@PTMC, LA, or PTMC for 72 h ($n = 3$). The GPR30 expression on different tumor stages of cholangiocarcinoma was shown (K for metastasis and L for primary tumor). DFS was shown between GPR30 high expression and low expression in patients with cholangiocarcinoma (M).

(N) Representative immunofluorescence images of GPR30 in the tumor tissues among all groups. Scale bars, 50 μm.

The comparisons among multiple groups were carried out using a parametric one-way ANOVA test, based on the normality results. Data are represented as mean ± SEM. $^*p < 0.05$.

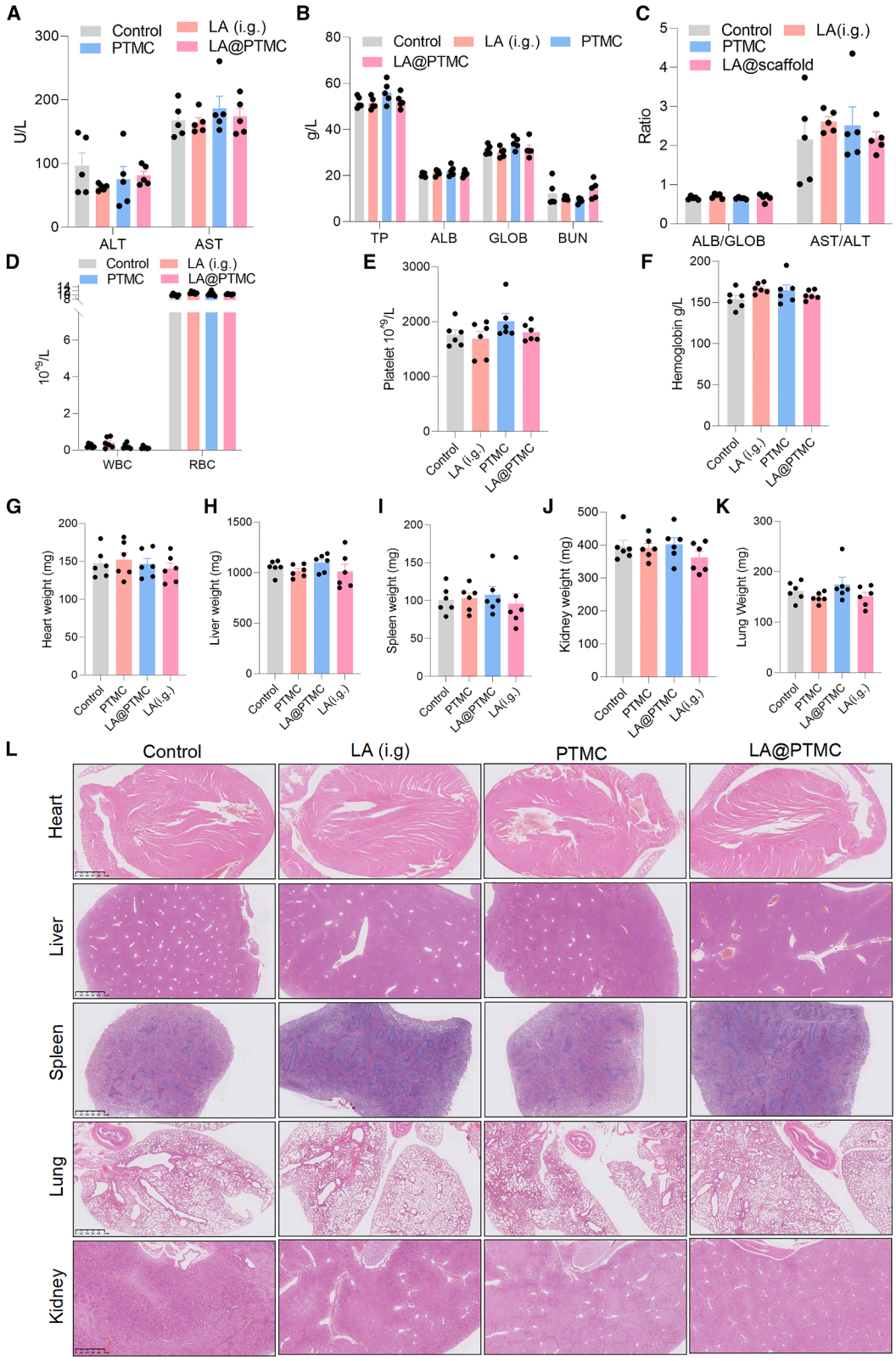

(legend on next page)

- Molecular docking (MD)
- QUANTIFICATION AND STATISTICAL ANALYSIS

SUPPLEMENTAL INFORMATION

Supplemental information can be found online at https://doi.org/10.1016/j.isci.2026.116093.

Received: August 25, 2025
Revised: January 30, 2026
Accepted: May 7, 2026

REFERENCES

1. Wang, C., Chen, L., Xu, C., Shi, J., Chen, S., Tan, M., Chen, J., Zou, L., Chen, C., Liu, Z., and Liu, X. (2020). A Comprehensive Review for Phytochemical, Pharmacological, and Biosynthesis Studies on Glycyrrhiza spp. Am. J. Chin. Med. *48*, 17–45. https://doi.org/10.1142/S0192415X20500020.
2. Li, M.T., Xie, L., Jiang, H.M., Huang, Q., Tong, R.S., Li, X., Xie, X., and Liu, H.M. (2022). Role of Licochalcone A in Potential Pharmacological Therapy: A Review. Front. Pharmacol. *13*, 878776. https://doi.org/10.3389/fphar.2022.878776.
3. Wu, J., Zhang, X., Wang, Y., Sun, Q., Chen, M., Liu, S., and Zou, X. (2018). Licochalcone A suppresses hexokinase 2-mediated tumor glycolysis in gastric cancer via downregulation of the Akt signaling pathway. Oncol. Rep. *39*, 1181–1190. https://doi.org/10.3892/or.2017.6155.
4. Wang, J., Zhang, Y.S., Thakur, K., Hussain, S.S., Zhang, J.G., Xiao, G.R., and Wei, Z.J. (2018). Licochalcone A from licorice root, an inhibitor of human hepatoma cell growth via induction of cell apoptosis and cell cycle arrest. Food Chem. Toxicol. *120*, 407–417. https://doi.org/10.1016/j.fct.2018.07.044.
5. Chen, G., Luo, S., Guo, H., Lin, J., and Xu, S. (2024). Licochalcone A alleviates ferroptosis in doxorubicin-induced cardiotoxicity via the PI3K/AKT/MDM2/p53 pathway. Naunyn-Schmiedebergs Arch Pharmacol *397*, 4247–4262. https://doi.org/10.1007/s00210-023-02863-1.
6. Yu, S.J., Cho, I.A., Kang, K.R., Jung, Y.R., Cho, S.S., Yoon, G., Oh, J.S., You, J.S., Seo, Y.S., Lee, G.J., et al. (2017). Licochalcone-E induces caspase-dependent death of human pharyngeal squamous carcinoma cells through the extrinsic and intrinsic apoptotic signaling pathways. Oncol. Lett. *13*, 3662–3668. https://doi.org/10.3892/ol.2017.5865.
7. Liu, J., Zhu, Z., Yang, Y., Adu-Frimpong, M., Chen, L., Ji, H., Toreniyazov, E., Wang, Q., Yu, J., and Xu, X. (2022). Preparation, characterization, pharmacokinetics, and antirenal injury activity studies of Licochalcone A-loaded liposomes. J. Food Biochem. *46*, e14007. https://doi.org/10.1111/jfbc.14007.
8. Xu, J., Zhuang, S., Liu, M., Wu, S., and Li, H. (2023). Prognostic effects of different malignant obstructive jaundice sites on percutaneous biliary intervention: A retrospective controlled study. J. Cancer Res. Therapeut. *19*, 78–85. https://doi.org/10.4103/jcrt.jcrt_2038_22.
9. Dhondt, E., Vanlangenhove, P., Geboes, K., Vandenabeele, L., Van Cauwenberghe, L., and Defreyne, L. (2020). No evidence of improved efficacy of covered stents over uncovered stents in percutaneous palliation of malignant hilar biliary obstruction: results of a prospective randomized trial. Eur. Radiol. *30*, 175–185. https://doi.org/10.1007/s00330-019-06374-7.
10. Siegel, R.L., Wagle, N.S., Cercek, A., Smith, R.A., and Jemal, A. (2023). Colorectal cancer statistics, 2023. CA Cancer J. Clin. *73*, 233–254. https://doi.org/10.3322/caac.21772.
11. Vibert, E., Canedo, L., and Adam, R. (2005). Strategies to treat primary unresectable colorectal liver metastases. Semin. Oncol. *32*, 33–39. https://doi.org/10.1053/j.seminoncol.2005.07.015.
12. Xing, D., Song, W., Gong, S., Xu, A., and Zhai, B. (2022). Analysis of the Bacterial Spectrum and Key Clinical Factors of Biliary Tract Infection in Patients with Malignant Obstructive Jaundice after PTCD. Dis. Markers *2022*, 1026254. https://doi.org/10.1155/2022/1026254.
13. Sportes, A., Camus, M., Greget, M., Leblanc, S., Coriat, R., Hochberger, J., Chaussade, S., Grabar, S., and Prat, F. (2017). Endoscopic ultrasound-guided hepaticogastrostomy versus percutaneous transhepatic drainage for malignant biliary obstruction after failed endoscopic retrograde cholangiopancreatography: a retrospective expertise-based study from two centers. Therapeut. Adv. Gastroenterol. *10*, 483–493. https://doi.org/10.1177/1756283X17702096.
14. Zhang, S., Huang, S., Xing, Z., Song, Y., and Yuan, F. (2025). Clinical effect of percutaneous hepatic puncture biliary drainage combined with metal stent implantation in the treatment of malignant obstructive jaundice. BMC Surg. *25*, 126. https://doi.org/10.1186/s12893-025-02807-x.
15. Lee, H., Won, D.S., Park, S., Park, Y., Kim, J.W., Han, G., Na, Y., Kang, M.H., Kim, S.B., Kang, H., et al. (2024). 3D-printed versatile biliary stents with nanoengineered surface for anti-hyperplasia and antibiofilm formation. Bioact. Mater. *37*, 172–190. https://doi.org/10.1016/j.bioactmat.2024.03.018.
16. Lee, T.H., Jung, M.K., Kim, T.K., Pack, C.G., Park, Y.K., Kim, S.O., and Park, D.H. (2019). Safety and efficacy of a metal stent covered with a silicone membrane containing integrated silver particles in preventing biofilm and sludge formation in endoscopic drainage of malignant biliary obstruction: a phase 2 pilot study. Gastrointest. Endosc. *90*, 663–672.e2. https://doi.org/10.1016/j.gie.2019.06.007.
17. Das, M., van der Leij, C., Katoh, M., Benten, D., Hendriks, B.M.F., and Hatzidakis, A. (2021). CIRSE Standards of Practice on Percutaneous Transhepatic Cholangiography, Biliary Drainage and Stenting. Cardiovasc. Interv. Radiol. *44*, 1499–1509. https://doi.org/10.1007/s00270-021-02903-4.
18. See, T.C. (2020). Acute biliary interventions. Clin. Radiol. *75*, 398.e9–398.e18. https://doi.org/10.1016/j.crad.2019.03.012.
19. Bordaçahar, B., Perdigao, F., Leblanc, S., Barret, M., Duchmann, J.C., Guillaumot, M.A., Chaussade, S., Scatton, O., and Prat, F. (2018). Clinical efficacy of anti-migration features in fully covered metallic stents for anastomotic biliary strictures after liver transplantation: comparison of conventional and anti-migration stents. Gastrointest. Endosc. *88*, 655–664. https://doi.org/10.1016/j.gie.2018.06.035.
20. Häner, J.D., Räber, L., and Windecker, S. (2019). Biodegradable vs. permanent polymer drug-eluting stents: the need for a new nomenclature to classify drug-eluting stent technology. Eur. Heart J. *40*, 2616–2619. https://doi.org/10.1093/eurheartj/ehz330.
21. Dumonceau, J.M., Tringali, A., Papanikolaou, I.S., Blero, D., Mangiavillano, B., Schmidt, A., Vanbiervliet, G., Costamagna, G., Devière, J., García-Cano, J., et al. (2018). Endoscopic biliary stenting: indications, choice

Figure 8. Safety evaluation of treatment with LA@PTMC *in vivo*

(A) Serum ALT and AST levels.
(B) Serum TP, ALB, GLOB, and BUN levels were analyzed.
(C) Ratios of ALB/GLOB and AST/ALT were shown.
(D–F) The counts of WBC and RBC (D), platelet (E), and hemoglobin (F) were detected.
(G–K) The weights of the heart (G), liver (H), spleen (I), kidney (J), and lung (K) were shown.
(L) H&E-stained images of heart, liver, spleen, lung, and kidney of mice after treatment was carried out. Scale bars, 1 mm.
The mouse was treated with PTMC, LA@PTMC, and LA (i.g) for 24 days. The comparisons among multiple groups were carried out using a parametric one-way ANOVA test, based on the normality results. Data are represented as mean ± SEM.

of stents, and results: European Society of Gastrointestinal Endoscopy (ESGE) Clinical Guideline - Updated October 2017. Endoscopy *50*, 910–930. https://doi.org/10.1055/a-0659-9864.

22. Xu, X.Y., Chen, Y.F., Tan, Q.G., Chen, Z.J., Li, Y., Wu, W.G., Wang, X.F., and Liu, Y.B. (2019). Construction of multilayer films with bactericidal and long-term antitumor drug release properties as a non-vascular stent coating for therapy in obstruction. J. Mater. Chem. B *7*, 4963–4972. https://doi.org/10.1039/c9tb01036j.
23. Khan, S.A., Rahman, Z.U., Javed, A., Ahmad, Z., Cai, Z., Jiang, O., and Xu, G. (2024). Natural biopolymers in the fabrication and coating of ureteral stent: An overview. Biomater. Adv. *165*, 214009. https://doi.org/10.1016/j.bioadv.2024.214009.
24. Asri, R.I.M., Harun, W.S.W., Hassan, M.A., Ghani, S.A.C., and Buyong, Z. (2016). A review of hydroxyapatite-based coating techniques: Sol-gel and electrochemical depositions on biocompatible metals. J. Mech. Behav. Biomed. Mater. *57*, 95–108. https://doi.org/10.1016/j.jmbbm.2015.11.031.
25. Zhang, W., Kanwal, F., Batool, A.I., Mustaqeem, M., Rehman, M.F.U., and Wan, X. (2022). Studying in vivo and in vitro effects of a novel polyvinyl benzyl chloride-D-glucaro-1, 4-lactonate polymer-coated bile duct stent for anti-biliary mud deposition. J. Appl. Biomater. Funct. Mater. *20*, 22808000221134988. https://doi.org/10.1177/22808000221134988.
26. Zan, R., Wang, H., Shen, S., Yang, S., Yu, H., Zhang, X., Zhang, X., Chen, X., Shu, M., Lu, X., et al. (2024). Biomimicking covalent organic frameworks nanocomposite coating for integrated enhanced anticorrosion and antifouling properties of a biodegradable magnesium stent. Acta Biomater. *180*, 183–196. https://doi.org/10.1016/j.actbio.2024.04.012.
27. Li, J., Qin, L., Feng, H., Zhang, Y., and Zhou, J. (2026). Data-Driven Machine Learning Framework for the Regulation of Protein Adsorption on Surfaces. Langmuir *42*, 1358–1371. https://doi.org/10.1021/acs.langmuir.5c05405.
28. Gu, Y., and Liang, C. (2024). TRAIP suppressed apoptosis and cell cycle to promote prostate cancer proliferation via TRAF2-PI3K-AKT pathway activation. Int. Urol. Nephrol. *56*, 1639–1648. https://doi.org/10.1007/s11255-023-03890-w.
29. Li, X., Tang, H., Tang, Q., and Chen, W. (2021). Decoding the Mechanism of Huanglian Jiedu Decoction in Treating Pneumonia Based on Network Pharmacology and Molecular Docking. Front. Cell Dev. Biol. *9*, 638366. https://doi.org/10.3389/fcell.2021.638366.
30. Liu, L., Mo, M., Chen, X., Chao, D., Zhang, Y., Chen, X., Wang, Y., Zhang, N., He, N., Yuan, X., et al. (2023). Targeting inhibition of prognosis-related lipid metabolism genes including CYP19A1 enhances immunotherapeutic response in colon cancer. J. Exp. Clin. Cancer Res. *42*, 85. https://doi.org/10.1186/s13046-023-02647-8.
31. Wang, J., He, Y., Maitz, M.F., Collins, B., Xiong, K., Guo, L., Yun, Y., Wan, G., and Huang, N. (2013). A surface-eroding poly(1,3-trimethylene carbonate) coating for fully biodegradable magnesium-based stent applications: toward better biofunction, biodegradation and biocompatibility. Acta Biomater. *9*, 8678–8689. https://doi.org/10.1016/j.actbio.2013.02.041.
32. Leung, J.W., Liu, Y.L., Chan, R.C.Y., Ling, T.K.W., and Cheng, A.F. (2002). Effects of adherence factors and human bile on bacterial attachment and biliary stent blockage: an in vitro study. Gastrointest. Endosc. *56*, 72–77. https://doi.org/10.1067/mge.2002.125366.
33. Leung, J.W., Liu, Y.L., Desta, T.D., Libby, E.D., Inciardi, J.F., and Lam, K. (2000). In vitro evaluation of antibiotic prophylaxis in the prevention of biliary stent blockage. Gastrointest. Endosc. *51*, 296–303. https://doi.org/10.1016/s0016-5107(00)70358-0.
34. Tang, H., Li, S., Zhao, Y., Liu, C., Gu, X., and Fan, Y. (2022). A surface-eroding poly(1,3-trimethylene carbonate) coating for magnesium based cardiovascular stents with stable drug release and improved corrosion resistance. Bioact. Mater. *7*, 144–153. https://doi.org/10.1016/j.bioactmat.2021.05.045.
35. Panoulas, V.F., Mastoris, I., Konstantinou, K., Tespili, M., and Ielasi, A. (2015). Everolimus-eluting stent platforms in percutaneous coronary intervention: comparative effectiveness and outcomes. Med. Devices *8*, 317–329. https://doi.org/10.2147/MDER.S66360.
36. Pan, C., Chen, H., and Yang, B. (2023). Licochalcone A Inhibits Proliferation and Metastasis of Colon Cancer by Regulating miR-1270/ADAM9/Akt/NF-kappaB axis. Iran. J. Public Health *52*, 1962–1972. https://doi.org/10.18502/ijph.v52i9.13578.
37. Darman, L., Kaurich, Q., Hassan, M.S., von Holzen, U., and Awasthi, N. (2025). Expanding Horizons in Cholangiocarcinoma: Emerging Targets Beyond FGFR2 and IDH1. Int. J. Mol. Sci. *26*, 10755. https://doi.org/10.3390/ijms262110755.
38. Nikhil Kumar Tej, J., Johnson, P., Krishna, K., Kaushik, K., Gupta, P.S.P., Nandi, S., and Mondal, S. (2021). Copper and Selenium stimulates CYP19A1 expression in caprine ovarian granulosa cells: possible involvement of AKT and WNT signalling pathways. Mol. Biol. Rep. *48*, 3515–3527. https://doi.org/10.1007/s11033-021-06346-5.
39. Gogola, J., Hoffmann, M., and Ptak, A. (2019). Persistent endocrine-disrupting chemicals found in human follicular fluid stimulate the proliferation of granulosa tumor spheroids via GPR30 and IGF1R but not via the classic estrogen receptors. Chemosphere *217*, 100–110. https://doi.org/10.1016/j.chemosphere.2018.11.018.
40. Chatterjee, S., Bose, S., Acharjee, S., Kundu, A., Tripathi, S.K., Ruiz de Porras, V., Zinzuwadia, S.S., and Bishayee, A. (2026). Oncopreventive and Oncotherapeutic Potential of Plant Secondary Metabolites Against Gastric Cancer: A Review. Phytother Res. *40*, 1354–1407.
41. Barros-Oliveira, M.D.C., Costa-Silva, D.R., Dos Santos, A.R., Pereira, R.O., Soares-Júnior, J.M., and Silva, B.B.d. (2021). Influence of CYP19A1 gene expression levels in women with breast cancer: a systematic review of the literature. Clinics *76*, e2846. https://doi.org/10.6061/clinics/2021/e2846.
42. Liu, D., Huo, X., Gao, L., Zhang, J., Ni, H., and Cao, L. (2018). NF-kappaB and Nrf2 pathways contribute to the protective effect of Licochalcone A on dextran sulphate sodium-induced ulcerative colitis in mice. Biomed. Pharmacother. *102*, 922–929. https://doi.org/10.1016/j.biopha.2018.03.130.
43. Wahida, A., Buschhorn, L., Fröhling, S., Jost, P.J., Schneeweiss, A., Lichter, P., and Kurzrock, R. (2023). The coming decade in precision oncology: six riddles. Nat. Rev. Cancer *23*, 43–54. https://doi.org/10.1038/s41568-022-00529-3.
44. Luo, Z., Fu, C., Li, T., Gao, Q., Miao, D., Xu, J., and Zhao, Y. (2021). Hypoglycemic Effects of Licochalcone A on the Streptozotocin-Induced Diabetic Mice and Its Mechanism Study. J. Agric. Food Chem. *69*, 2444–2456. https://doi.org/10.1021/acs.jafc.0c07630.
45. Zeng, G., Shen, H., Yang, Y., Cai, X., and Xun, W. (2014). Licochalcone A as a potent antitumor agent suppresses growth of human oral cancer SCC-25 cells in vitro via caspase-3 dependent pathways. Tumour Biol. *35*, 6549–6555. https://doi.org/10.1007/s13277-014-1877-1.
46. Heise, T., Sawyer, A.Y., Hirai, T., Schaible, S., Sy, H., and Wickramasekara, S. (2022). Report on investigation of ISO 10993-12 extraction conditions. Regul. Toxicol. Pharmacol. *131*, 105164. https://doi.org/10.1016/j.yrtph.2022.105164.
47. Tomczak, K., Czerwińska, P., and Wiznerowicz, M. (2015). The Cancer Genome Atlas (TCGA): an immeasurable source of knowledge. Contemp. Oncol. *19*, A68–A77. https://doi.org/10.5114/wo.2014.47136.
48. Liu, Z., Liu, L., Weng, S., Xu, H., Xing, Z., Ren, Y., Ge, X., Wang, L., Guo, C., Li, L., et al. (2023). BEST: a web application for comprehensive biomarker exploration on large-scale data in solid tumors. Journal of Big Data *10*, 1.
49. Daina, A., Michielin, O., and Zoete, V. (2019). SwissTargetPrediction: updated data and new features for efficient prediction of protein targets of small molecules. Nucleic Acids Res. *47*, W357–W364. https://doi.org/10.1093/nar/gkz382.
50. Deshpande, N., Addess, K.J., Bluhm, W.F., Merino-Ott, J.C., Townsend-Merino, W., Zhang, Q., Knezevich, C., Xie, L., Chen, L., Feng, Z., et al. (2005). The RCSB Protein Data Bank: a redesigned query system and relational database based on the mmCIF schema. Nucleic Acids Res. *33*, D233–D237. https://doi.org/10.1093/nar/gki057.

STAR★METHODS

KEY RESOURCES TABLE

REAGENT or RESOURCE	SOURCE	IDENTIFIER
Antibodies		
AKT Antibody	MedChemExpress	Cat#HY-P80535, lot#554088
Aromatase Antibody	MedChemExpress	Cat#HY-P80547, lot#315842
GPR30 Antibody	MedChemExpress	Cat#HY-P81150 lot#665320
Ki67 Antibody	MedChemExpress	Cat#HY-P80506, lot#339090
Chemicals, peptides, and recombinant proteins		
Licochalcone A	Chengdu Alfa Biotechnology Co., Ltd.	CAS No. 58749-22-7, Lot: AZEE2602
Deposited data		
Raw data	This paper;BMDC	https://www.biosino.org/node/home accession number:OEP00006442
Mendeley Data	Mendeley Data	https://doi.org/10.17632/9vx86938md.1
Experimental models: Cell lines		
RBE cells	National Collection of Authenticated Cell Cultures	CSTR:19375.09.3101HUMTCHu179
HCT116 cells	National Collection of Authenticated Cell Cultures	CSTR:19375.09.3101HUMSCSP5076

EXPERIMENTAL MODEL AND STUDY PARTICIPANT DETAILS

Cell culture

RBE cells (National Collection of Authenticated Cell Cultures; TCHu179, CSTR:19375.09.3101HUMTCHu179) and HCT116 cells (National Collection of Authenticated Cell Cultures; SCSP-5076, CSTR:19375.09.3101HUMSCSP5076) were obtained commercially and cultured according to the manufacturer's protocols. Cell line identity was authenticated by short tandem repeat (STR) profiling (Genewiz, Inc.), and all cells tested negative for mycoplasma contamination. They were cultured in high-glucose Dulbecco's Modified Eagle's Medium (DMEM) (C11885500BT, Gibco, Germany). The medium was supplemented with 10% fetal bovine serum (FBS) (C04001, VivaCell, China) and 1% antibiotic-antimycotic (C100C8, NCM Biotech, Suzhou, China). HUVECs cells and RAW264.7 cells were cultured in an incubator (Thermo, USA) at 37°C with 5% CO_2. HCT116 cells were included to model secondary biliary obstruction caused by colorectal cancer liver metastases, a clinically relevant scenario in patients requiring biliary stenting.

Animal experiments

Thirty-two male BALB/c nude mice (4 weeks old, 12–15 g) were purchased from Hangzhou Qizhen Experimental Animal Technology Co., Ltd. All animal procedures and experimental protocols were approved by the Animal Ethics and Welfare Committee of Zhejiang Chinese Medical University (Approval No.: IACUC-20240909-09) and conducted in strict accordance with the guidelines of the National Institutes of Health (NIH) Guide for the Care and Use of Laboratory Animals. Mice were acclimatized for one week under specific pathogen-free (SPF) conditions (23 ± 2°C, 50% relative humidity, 12-h light/dark cycle) with *ad libitum* access to food and water.

First, eight nude mice were used for primary tumor establishment: RBE cell suspension (100 μL, approximately 5.0×10^6 cells) was subcutaneously injected into the right axilla. When the average tumor volume exceeded 1500 mm^3 (calculated using the formula: Volume = 0.5 × length × $width^2$) or the maximum diameter exceeded 15 mm, the mice were euthanized and tumors were aseptically harvested. Subsequently, the remaining 24 nude mice were used for secondary transplantation modeling: following anesthesia via intraperitoneal injection of sodium pentobarbital (60 mg/kg), the harvested tumor tissue was cut into fragments of approximately 27 mm^3 (3 × 3 × 3 mm) and subcutaneously implanted into the right axilla of each mouse.

The 24 tumor-bearing mice were randomly divided into four experimental groups (n = 6 per group): (1) Control group (received only tumor implantation without any further intervention); (2) LA (oral gavage) group: administered LA at 10 mg/kg daily by oral gavage in the morning, with the dose selected based on previous studies[44,45]; (3) PTMC group: received an 8 × 8 mm PTMC-coated stent implanted subcutaneously adjacent to the tumor site at the time of tumor fragment implantation; (4) LA@PTMC group: received an 8 × 8 mm LA-loaded PTMC-coated stent implanted subcutaneously adjacent to the tumor site simultaneously with tumor implantation. The implanted materials remained in the mice until the end of the experiment.

Starting from day 7 post-implantation (when tumors became macroscopically visible), body weight and tumor dimensions were measured every three days. The experiment was terminated when the average tumor volume in any group reached approximately

1500 mm^3 or the maximum tumor diameter exceeded 15 mm. All mice were then euthanized. Whole blood was collected for serum separation, and tumor tissues along with major organs were harvested for subsequent analyses.

METHOD DETAILS

LA@PTMC preparation

First, NITI alloy was fabricated into thin sheets with dimensions of 10 cm × 10 cm × 0.5 mm (length × width × thickness). To obtain a smooth surface with uniformly oriented scratches, the samples were sequentially polished using 800#, 1500#, and 2000# waterproof abrasive papers. The polished samples were then subjected to ultrasonic cleaning in acetone for 30 minutes to remove surface oil, followed by drying. Subsequently, they were ultrasonically cleaned in absolute ethanol for 20 minutes and dried again for further use.

The NITI samples were then subjected to anodic oxidation using a two-electrode electrochemical system, consisting of a graphite sheet as the cathode and a metal holder with the sample as the anode. The electrolyte was composed of 0.104 M ammonium fluoride (NH_4F), acetone (C_3H_6O), and distilled water (H_2O). The oxidation was carried out at room temperature (approximately 295 K), with the electrode distance maintained at around 10 mm. A constant anodic voltage of 30 V was applied for 12 hours. The resulting samples with micro-porous surfaces were designated as anodizing PEO.

Subsequently, PTMC was dissolved in tetrahydrofuran (THF) at a concentration of 2.5% (w/w) and stirred thoroughly at room temperature to obtain a homogeneous PTMC-THF solution. Based on this solution, LA (CAS No. 58749-22-7, Lot: AZEE2602) was added to achieve a final concentration of 1 mg/mL, resulting in the LA@PTMC coating solution. The LA used in this study was a commercially available compound purchased from Chengdu Alfa Biotechnology Co., Ltd. (China), with a certified purity of ≥98%. The compound was not isolated or synthesized in-house; no further purification or structural optimization was performed prior to use. The solution was applied to the surface of anodizing PEO samples using a dip-coating method: each dip lasted 5 minutes and was repeated three times. The resulting samples were designated as LA@PTMC. As a control, a PTMC-THF solution without LA was applied to anodizing PEO samples using the same procedure. These samples were designated as PTMC.

The surface morphology of the samples was characterized using a scanning electron microscope (SEM, Thermo Fisher Scientific, USA) to observe their micro- and nanostructural features. Meanwhile, an energy-dispersive X-ray spectroscopy (EDS) system attached to the SEM was employed to analyze the elemental composition and corresponding weight percentages of the sample surfaces, to assess elemental distribution and compositional uniformity.

In addition, atomic force microscopy (AFM, Bruker, Germany) in tapping mode was used to perform three-dimensional surface topography analysis, providing information on surface profiles and roughness.

Extract preparation as follows: LA@PTMC or PTMC stent was immersed into 10%FBS DMEM medium at 1.25cm^3/mL for 72h according to ISO-10993 guideline.[46] Afterward, the extract was harvested and filtered with 0.22μm filter for ready to use.

Water contact angle test

A dynamic contact angle measuring instrument (JC2000C1, Shanghai, China) was used to determine the water contact angle (WCA) of the sample surfaces. The measurements were conducted at room temperature. A total of 500 μL of pure water was loaded into a microsyringe, and 2 μL droplets were gently dispensed onto the sample surface at an injection rate of 1 μL/s. The wettability of the material surface was evaluated based on the contact angle (θ), with $\theta = 85^\circ$ serving as the boundary between hydrophilicity and hydrophobicity: surfaces with $\theta < 85^\circ$ were considered hydrophilic, while those with $\theta > 85^\circ$ were considered hydrophobic.

Encapsulation efficiency and drug loading of LA on NITI

To evaluate the drug-loading capacity of the NITI alloy, LA was loaded onto the alloy surface, and the encapsulation efficiency (EE%) and drug loading (DL%) were determined. Briefly, the concentration of free LA was measured using UV–vis spectrophotometry at its characteristic absorption wavelength of 372 nm. The amount of drug loaded onto the NITI alloy was calculated by subtracting the free drug from the total initial drug.

The encapsulation efficiency (EE%) and drug loading (DL%) were calculated using the following formulas:

$$EE\ \% = \frac{m_{total}\text{-}m_{free}}{m_{total}} \times 100\%$$

$$DL\ \% = \frac{m_{loaded}}{m_{carrier}} \times 100\%$$

In this study, the EE% and DL% of LA on the NITI alloy were determined to be 22.5% and 5.11%, respectively.

Drug release study of LA

The *in vitro* release behavior of LA from NITI alloy coated with LA@PTMC was evaluated using UV–Vis spectrophotometry. Samples were immersed in 10 mL of PBS or simulated body fluid (SBF) and incubated at 37 °C under gentle shaking (approximately 80–100 rpm) to simulate physiological conditions. At predetermined time intervals (e.g., 6, 12, 24, 48, 72, and 96 hours), 1 mL of the release medium was withdrawn and replaced with an equal volume of fresh medium to maintain sink conditions. The

concentration of LA in the collected samples was determined using a UV–Vis spectrophotometer at its characteristic absorption wavelength of 372 nm.

Cell proliferation assay

RBE and HCT116 cells were then exposed to LA at specified concentrations or extract of PTMC or LA@PTMC for 5 days recorded by light microscopy. Cell viability was assessed using the CCK-8 assay kit (Beyotime Biotechnology, China; C0037) according to manufacturer specifications: 10 μL CCK-8 reagent was added per 100 μL culture medium, followed by incubation at 37°C for 2.5 hours protected from light. Absorbance was measured at 450 nm using a microplate reader, with viability calculated. All experiments included vehicle controls and were performed in technical triplicates with three biological replicates. Dose-response curves were generated using nonlinear regression analysis (GraphPad Prism v9.0).

Bioinformatics database analysis

In this study, the indicated gene expression, survival or other patients with Cholangiocarcinoma were analyzed based on TCGA (https://www.cancer.gov/ccg/research/ genome-sequencing/tcga),[47] and BEST (https://rookieutopia.hiplot.com.cn/app_direct/BEST/#) database.[48] The potential target of LA was screen out with SwissTargetPrediction database (http://www.swisstargetprediction.ch/).[49]

Lactate dehydrogenase (LDH) release assay

Cytotoxicity was assessed by quantifying plasma membrane integrity via LDH release. Tumor cells (RBE, HCT116) in logarithmic growth phase were seeded in 96-well plates at 1X 10^4cells/well and allowed to adhere overnight. Cells were then exposed to experimental treatments (LA@PTMC extracts, free LA, PTMC extracts) or controls for 24h. Following treatment, 100 μL of supernatant per well was carefully transferred to a fresh 96-well plate. LDH activity was measured using a commercial LDH Cytotoxicity Assay Kit (Thermo Fisher Scientific, Pierce™) according to the manufacturer's protocol. Briefly, 50 μL of supernatant was incubated with 50 μL of reaction mixture for 30 minutes at room temperature, protected from light. The reaction was stopped by adding 50 μL of stop solution. Absorbance was read at 490 nm using a microplate reader. Controls included: untreated cells (spontaneous LDH release), lysis buffer-treated cells (maximum LDH release, 45 min before supernatant collection), and medium-only background. Cytotoxicity percentage was calculated using the formula:

$$\%\ \text{Cytotoxicity} = [(\text{Test Sample} - \text{Spontaneous Release}) / (\text{Maximum Release} - \text{Spontaneous Release})] \times 100.$$

Experiments were repeated at least three times independently.

Clone formation assay

RBE and HCT116 cells were harvested during logarithmic growth phase using 0.25% trypsin-EDTA. Single-cell suspensions were verified microscopically. Cells were seeded into 6-well culture plates at densities optimized per cell line (500 cells/well) to yield colonies per well in untreated controls. After allowing 6-8 hours for attachment, cells were exposed to experimental treatments LA@PTMC extracts, free LA, PTMC extracts, or control) for 10 days and changed same medium every three day. Colonies were fixed with 4% paraformaldehyde (15 m in), stained with 0.5% (w/v) crystal violet (30 min), and thoroughly rinsed with distilled water. The plates were captured with a camera.

RNA-seq analysis

For high-throughput sequencing, total RNA extracted from two biological replicates (Control and LA@PTMC tumor tissues) was submitted to the LC-Bio Technologies (Hangzhou,China) Co., Ltd. for library preparation and RNA-seq. Briefly, cells treated in 6-well plates were harvested, and total RNA was isolated from tumor tissues using Trizol reagent. mRNA was enriched via poly-A selection, and 50 base-pair paired-end sequencing was performed on the BGISEQ-500 platform. Raw reads were filtered using SOAP and SOAPnuke. Clean reads were then aligned to the RefSeq transcriptome database using Bowtie2. Gene expression levels were quantified as FPKM (fragments per kilobase of transcript per million mapped reads). Differentially expressed genes (DEGs) were identified through pairwise comparisons, applying thresholds of a fold change > 2 and a false discovery rate (FDR) < 0.001. Samples were clustered based on similarity and visualized in a dendrogram. DEGs were functionally classified using KEGG pathway analysis, GSEA (Gene Set Enrichment Analysis), and heatmap visualization.

Cell scratching test

RBE and HCT116 were seeded into 6-well plate at $5\times10^{\hat{}5}$ cells per well. After Cell confluence reached 90%, plates were scratched with pipette tips, washed with PBS and added with extracts or LA. Cells were captured by light microscope at 0h and 18h. The migration ability of RBE and HCT116 cells was quantified by subtracting the scratch distance at 0h from the area 18h, respectively, with ImageJ 1.46 software.

Cell cycle by flow cytometry (FC) analysis

After co-culture with the PTMC or LA@PTMC extracts or indicated LA concentration for 72h, RBE or HCT116 cells were collected, washed once with PBS, fixed in ice-cold 70% ethanol and stored at -20°C overnight. Afterwards, cells were washed again with PBS and suspended in 400 μL PBS containing 100μg/mL RNase A and 150μg/mL propidium iodide (PI, Beyotime, China). Finally, after 4°C incubation for 30min, cells were collected and subjected for flow cytometry (BD, USA). Data was analyzed with Flowjo software.

Safety evaluation *in vivo*

For hematological analysis, 150 μL of whole blood samples collected from mice were analyzed using a Sysmex-XN1000 fully automated hematology analyzer to determine red blood cell count (RBC), white blood cell count (WBC), platelet count, and hemoglobin concentration. For serum biochemical analysis, 120 μL of serum samples were assessed using a Hitachi 3100 fully automated biochemistry analyzer to measure levels of alanine aminotransferase (ALT), aspartate aminotransferase (AST), total protein (TP), albumin (ALB), globulin (GLOB), and blood urea nitrogen (BUN). Additionally, the ALB/GLOB ratio and AST/ALT ratio were calculated and compared.

Immunofluorescence (IF) staining

Following deparaffinization, paraffin-embedded tissue sections underwent heat-induced antigen retrieval in 1× citrate sodium buffer (pH 6.0) at approximately 95°C for 20 minutes. After cooling to room temperature, non-specific binding sites were blocked with 5% Bovine Serum Albumin (BSA) for 30 minutes. Sections were then incubated overnight at 4°C with primary antibodies targeting KI67(HY-P80506, lot#339090, MedChemExpress), AKT (HY-P80535, lot#554088, MedChemExpress), CYP19A1(HY-P80547, lot#315842, MedChemExpress), and GPR30(HY-P81150 lot#665320, MedChemExpress). The next day, the unbound primary antibody was removed by washing three times (5 minutes each) with (PBS), followed by incubation with an appropriate horseradish peroxidase (HRP)-conjugated secondary antibody for 1 hour at room temperature in the dark. After three additional PBS washes, target detection was performed using Tyramide Signal Amplification (TSA) according to the manufacturer's protocol. Sections were subsequently washed three times in PBS, and cell nuclei were counterstained with 4',6-diamidino-2-phenylindole (DAPI) in the dark. Finally, sections were mounted using an anti-fade mounting medium to preserve fluorescence, and images were acquired using a fluorescence inverted microscope (ZEISS, Germany).

Real-time quantitative polymerase chain reaction (RT-qPCR)

According to the manufacturer's protocols, total RNA was extracted from HCT116 and RBE cells using a commercial RNA extraction kit. Subsequently, the extracted total RNA was reverse transcribed into complementary DNA (cDNA) using a reverse transcription kit. The cDNA was then amplified via a three-step polymerase chain reaction protocol on a real-time quantitative PCR instrument, with the specific cycling conditions as follows: initial denaturation at 95°C for 5 min, followed by 40 cycles of denaturation at 95°C for 10 s, annealing at 60°C for 20 s, and extension at 72°C for 20 s. Gene-specific primers synthesized by Sunya Biotech were used, with sequences as follows:

AKT:

Forward:5'-CACTTTCGGCAAGGTGATCC-3', Reverse:5'-GTCCTGGCCACGATGACTT-3'; GPR30:

Forward:5'-GAGGTGTACCTCTGCTGGAC-3', Reverse:5'-CCTGGAAGCCTCCTTGGTCA-3';

β-actin:

Forward: 5'-AAGGATTCCTATGTGGGCGAC-3',

Reverse: 5'-CGTACAGGGATAGCACAGCC-3'.

Relative quantification of target gene expression levels was determined using the $2^{-\Delta\Delta Ct}$ method, normalized to the endogenous control gene β-actin.

Hematoxylin and eosin (H&E) staining

Tumor tissues and representative major organs were fixed in 4% paraformaldehyde (PFA) for 24 hours at room temperature, followed by dehydration through a graded ethanol series, clearing in xylene, and embedding in paraffin blocks. Sections of 4 μm thickness were cut using a rotary microtome, mounted on glass slides, and dried overnight. For staining, sections were deparaffinized in xylene and rehydrated through a descending ethanol gradient. Nuclei were stained with Mayer's hematoxylin for 8–10 minutes, rinsed in running tap water, and differentiated in 1% acid alcohol. Cytoplasmic counterstaining was performed using 0.5% eosin Y solution for 1–2 minutes. After dehydration through an ascending alcohol series and clearing in xylene, sections were cover slipped with neutral balsam mounting medium. Histopathological evaluation was conducted under a light microscope, and digital images of all samples were systematically documented for morphological analysis.

Western Blot (WB)

Total protein was extracted from HCT116 and RBE cells according to standard procedures (typically using RIPA or similar lysis buffer). Protein samples were separated by electrophoresis on 10% SDS-polyacrylamide gels and subsequently transferred onto polyvinylidene difluoride (PVDF) membranes. The membranes were blocked with non-fat dry milk for 1 hour at room temperature to prevent non-specific binding. Following blocking, the membranes were incubated overnight at 4°C with primary antibodies

specific for AKT (HY-P80535, lot#554088, MedChemExpress), CYP19A1(HY-P80547, lot#315842, MedChemExpress), and GPR30(HY-P81150 lot#665320, MedChemExpress) under gentle agitation. The next day the unbound primary antibody was removed by washing the membranes three times (10 minutes per wash). Membranes were then incubated with appropriate horseradish peroxidase (HRP)-conjugated species-specific secondary antibodies for 1 hour at room temperature. After three additional washes, protein bands were detected using enhanced chemiluminescence (ECL) substrate and visualized on a chemiluminescent imaging system. Relative protein expression levels, normalized to β-actin or GAPDH (as appropriate for the experiment), were quantified using ImageJ software.

Cellular thermal shift assay (CETSA)

RBE cells were lysed using NP-40 lysis buffer, and the prepared cell lysates were incubated with 25 μM LA at 4°C for 4 hours. The lysate was then divided into ten equal aliquots. Each aliquot was incubated at a designated temperature (37, 41, 45, 49, 53, 57, 61, 65, 69, or 73°C) for 4 minutes, followed by centrifugation at 4°C and 12,000 g for 10 minutes. The supernatants were transferred to fresh microcentrifuge tubes and mixed with 2.5×loading buffer. After denaturation (99°C, 10 minutes), protein samples were analyzed by Western blot to detect the expression levels of CYP19A1.

Microscale Thermophoresis (MST) analysis

Molecular interactions were quantified by MST. Briefly, his-tagged protein (human his-CYP19A1) was cultured with serial dilutions of LA in buffer (PBS + 0.1% Tween-20) for 30min. Samples were loaded into capillaries, and an infrared laser locally heated the solution, inducing thermophoresis. The ligand concentration-dependent changes of normalized fluorescence (ΔFnorm) were detected. Dissociation constants (KD) were determined by fitting the binding curve (NanoTemper Monolith instrument).

Molecular docking (MD)

To predict the interactions between LA and CYP19A1, molecular docking simulations were carried out using AutoDock 4.2.6. The three-dimensional structure of LA (PubChem CID: 5318998) was retrieved from PubChem. Although no quantum mechanical geometry optimization (e.g., DFT) was performed, the ligand underwent standard preparation in AutoDock Tools, including assignment of Gasteiger partial charges, detection of rotatable bonds, and energy minimization using the built-in force field to generate a low-energy conformation suitable for docking.

The crystal structure of human CYP19A1 (PDB ID: 3S79) was obtained from the RCSB Protein Data Bank.[50] Prior to docking, the protein was prepared by removing co-crystallized ligands and water molecules, adding polar hydrogens, merging non-polar hydrogens, and assigning Kollman united-atom charges.

A grid box of 60 × 60 × 60 Å (spacing: 0.375 Å) was centered on the heme cofactor—the catalytic core of CYP19A1—to encompass the substrate-binding pocket. Docking simulations employed the Lamarckian Genetic Algorithm with 100 independent runs and a maximum of 25,000,000 energy evaluations per run. The resulting poses were clustered based on a root-mean-square deviation threshold of 2.0 Å, and the top-scoring pose (lowest predicted binding free energy, ΔG in kcal/mol) was selected for interaction analysis.

Ligand-protein interactions were visualized using Discovery Studio 2021. Hydrogen bonds (distance $\leq$ 3.5 Å, angle $\geq$ 120°), hydrophobic contacts, and π-π stacking interactions were characterized. A heat map of interaction frequencies across the top 10 clusters was generated to identify conserved binding features.

QUANTIFICATION AND STATISTICAL ANALYSIS

All experiments were repeated at least three times independently and were analyzed using SPSS software (Version 20, IBM Co. USA). Differences among groups were analyzed by one-way ANOVA with Tukey HSD or Dunnett T3 methods. All results were interpreted as means ± SEM. $^{*}p < 0.05$ was considered as statistical significance.